Rapid endothelial infection, endothelialitis and vascular damage characterise SARS-CoV-2 infection in a human lung-on-chip model

Vivek V Thacker *[1], Kunal Sharma^[1], Neeraj Dhar ^[1], Gian-Filippo Mancini[2], Jessica Sordet-Dessimoz[2], John D McKinney[1]

[1]Global Health Institute, Ecole Polytechnique Federale de Lausanne, Switzerland

[2] Histology Core Facility, Ecole Polytechnique Federale de Lausanne, Switzerland

^ equal contribution

*Corresponding author: Vivek V Thacker, vivekvthacker@gmail.com

Abstract

Severe cases of COVID-19 present with hypercoagulopathies and systemic endothelialitis of the lung microvasculature. The dynamics of vascular damage, and whether it is a direct consequence of endothelial infection or an indirect consequence of immune cell mediated cytokine storms is unknown. This is in part because *in vitro* models are typically epithelial cell monocultures or fail to recapitulate vascular physiology. We use a vascularised lung-on-chip model where, consistent with monoculture reports, low numbers of SARS-CoV-2 virions are released apically from alveolar epithelial cells. However, rapid infection of the underlying endothelial layer leads to the generation of clusters of endothelial cells with low or no CD31 expression, a progressive loss of endothelial barrier integrity, and a pro-coagulatory microenvironment. These morphological changes do not occur if these cells are exposed to the virus apically. Viral RNA persists in individual cells, which generates a response that is skewed towards NF-KB mediated inflammation, is typified by IL-6 secretion even in the absence of immune cells, and is transient in epithelial cells but persistent in endothelial cells. Perfusion with Tocilizumab, an inhibitor of trans IL-6

signalling slows the loss of barrier integrity but does not prevent the formation of endothelial cell clusters with reduced CD31 expression. SARS-CoV-2 mediated endothelial cell damage occurs despite a lack of rapid viral replication, in a cell-type specific manner and independently of immune-cell mediated cytokine storms, whose effect would only exacerbate the damage.

33 **Introduction**

34 Organ-on-chip technologies recreate key aspects of human physiology in a bottom-up
35 and modular manner[1]. In the context of infectious diseases, this allows for studies of
36 cell dynamics[2,3], infection tropism[4], and the role of physiological factors in disease
37 pathogenesis in more native settings[5]. This is particularly relevant for the study of
38 respiratory infectious diseases[6], where the vast surface area of the alveoli poses a
39 challenge to direct experimental observation.

40 COVID-19, caused by the novel *betacoronavirus* SARS-CoV-2, first manifests as an
41 infection of the upper airways. Severe cases are marked by progression into the lower
42 airways and alveoli. Here, it manifests as an atypical form of acute respiratory distress
43 syndrome (ARDS) characterized by good lung compliance measurements[7,8], and
44 elevated levels of coagulation markers such as D-dimers[9], and pro-inflammatory
45 markers in the blood[10]. Autopsy reports show numerous microvascular thrombi in the
46 lungs of deceased patients together with evidence of the intracellular presence of the
47 virus in vascular cells[11,12]. These reports suggest that infection of and alterations to
48 lung microvasculature plays a key role in COVID-19 pathogenesis[13,14], which is further
49 reinforced by the early observation of endothelial cell damage, platelet aggregation and
50 the formation of microthrombi in an ante-mortem study[15]. Yet most *in vitro* studies
51 have focused on monocultures of upper airway respiratory cells. In studies with alveolar
52 epithelial cells, SARS-CoV-2 has been shown to replicate poorly both in the A549 lung
53 adenocarcinoma cell line[16] and in primary alveolar epithelial cells *ex vivo*[17] and has
54 been reported to be unable to infect primary lung microvascular endothelial cells[18],
55 which are at odds with the reported medical literature. There is therefore an urgent need
56 for a better understanding of the pathogenesis of SARS-CoV-2 in alveolar epithelial
57 cells, especially in a more realistic model of the alveolar space that is vascularized. The

58 lung-on-chip model is well-suited to this purpose because it includes a vascular
59 compartment maintained under flow, and infection can occur at the air-liquid
60 interface[19], two key physiological features that are lacking in organoid models[20–22]. We
61 therefore establish a human lung-on-chip model for SARS-CoV-2 infections, and probe
62 the viral growth kinetics, cellular localization and responses to a low dose infection
63 using qRT-PCR, ELISA, RNAScope, immunofluorescence and confocal imaging (Fig.
64 S1A).
65
66 **Results**
67 **SARS-CoV-2 infection of a human lung-on-chip alters expression of viral entry**
68 **factors**
69 A human lung-on-chip (LoC) model for SARS-CoV-2 pathogenesis (Fig. 1A) mimics
70 the alveolar space using primary human alveolar epithelial cells ('epithelial') and lung
71 microvascular endothelial cells ('endothelial'), which form confluent monolayers on
72 the apical and vascular sides of the porous membrane in the chip (Fig. 1B, C). The
73 modular nature of the technology allowed us to recreate otherwise identical LoCs either
74 without ('w/o') (Fig. 1B) or with the addition of CD14+ macrophages (representative
75 image in Fig. S1B) to the epithelial layer on the apical side of the chip. The latter
76 configuration was used for a subset of experiments as indicated throughout the text. We
77 first characterized the epithelial and endothelial cells used, both in monoculture and on-
78 chip at the air-liquid interface to verify that the cells mimicked human alveolar
79 physiology. In epithelial cells, *ACE2* expression was low both in monoculture (Fig
80 S2A) and on-chip (Fig. 1E) consistent with transcriptomic[18,23] and proteomic analyses[24]
81 of human tissue. Expression on-chip was five-fold lower than in monoculture (Fig.
82 S2B). Low *ACE2* expression was also observed from RNAscope assays on uninfected

83 LoCs (Fig. 1D). Although *ACE2* expression was particularly low in endothelial cells in
84 monoculture (Fig. S2A, expression increased 10-fold on-chip (Fig. S2B) so that levels
85 in epithelial and endothelial cells were comparable (Fig. 1E). This upregulation in
86 *ACE2* expression could possibly be due to the effects of shear stress and flow in the
87 vascular channel[25]. Neuropilin-1, an integrin-binding protein[26] has recently been
88 reported to be an alternative receptor for SARS-CoV-2 entry[27,28] that is highly
89 expressed in pulmonary microvascular cells. Consistent with these reports, *NRP1*
90 expression was between one and four orders of magnitude higher than *ACE2* expression
91 in both cell types in monoculture (Fig. S2A) and on-chip (Fig. 1E). On-chip, *NRP1*
92 expression was 6-fold higher in endothelial cells compared to epithelial cells (Fig S2B).
93 Lastly, mature alveolar epithelial cells retained differentiation in type I and type II cells,
94 which we verified by immunostaining for type II (pro-SPC) and type I (Podoplanin)
95 markers in monocultures (Fig. S3A-C) as well as through qRT-PCR measurements for
96 type II (*ABCA3*, *SFTPC*) and type I (*AQP5*, *PDPN*, *CAV1*) markers in cells from the
97 epithelial layer of uninfected LoCs (Fig. S3D). Endothelial cells showed characteristic
98 expression of Platelet Endothelial Cell Adhesion Molecule (PECAM-1 or CD31) at cell
99 junctions (Fig. 1C, additional images in Fig. 4C, D).
100
101 A low dose infection (200-300 plaque forming units (PFUs), multiplicity of infection
102 (MOI)=0.003) of the apical surface of the LoC resulted in decreases in *ACE2* expression
103 in epithelial and *NRP1* expression in both epithelial and endothelial cells at 1 dpi (Fig.
104 1F, I). Expression of both cell surface receptors remained downregulated at 3 dpi (Fig.
105 1J). These results are consistent with observations using RNAscope assays, where
106 *ACE2* levels in the epithelial layer declined over subsequent days (Fig. 1D, G, H,
107 p=0.014). On the other hand, infection resulted in increased expression of the

108 TMPRSS2 protease[29] required to cleave the spike protein for viral entry at 1 dpi in both
109 cell types relative to uninfected controls (Fig. 1 F, I), with variable expression levels
110 across chips. This trend was also maintained at 3 dpi (Fig. 1J). Overall, these results
111 show that both ACE2 and NRP1 likely play a role in pathogenesis in the alveolar space,
112 aided by increased TMPRSS2 levels. In comparison, infection did not alter levels of
113 type II or type I alveolar epithelial cell markers significantly (Fig. S3E, F).
114
115 **Infection of the alveolar space is characterized by a lack of productive infection,**
116 **slow intracellular replication, and transmission to the endothelial layer**
117 We first characterized the progression of infection by measuring the release of viral
118 genomes via qRT-PCR and the number of infectious virions released via measurement
119 of plaque forming units (PFUs). Infected LoCs were monitored daily for the release of
120 infected viral progeny (1) *apically* – on the epithelial layer and (2) in the cell culture
121 media flowed through the vascular channel ('apical wash' and 'vascular effluent' in
122 Fig. 1A). A low number of viral genomes were released apically from the epithelial
123 layer, and the number of genomes detected decreased over 1-3 dpi (Fig. 2A). Genome
124 copy numbers were 100-fold lower than the starting inoculum (between 200-300 PFU).
125 Low numbers of infectious virions were also detected via measurements of PFU from
126 eight LoCs w/o macrophages at 1 dpi and two LoCs w/o macrophages at 2 dpi (Fig.
127 2B). These results showed that, on the whole, productive infection of the epithelial cell
128 layer did not occur on-chip, although instances of small numbers of epithelial cells with
129 high levels of spike protein (Fig. S5A) or viral genomic RNA (Fig. S9) were detected
130 via microscopy and likely contribute to the low levels of infectious virions released.
131 No viral genomes were detected in the vascular effluent (Fig. 2B), and the lack of
132 infectious particles in the effluent was confirmed for two LoCs with and w/o

133 macrophages by plaque forming unit assays (data not shown). This ruled out the
134 possibility of direct release of virions from the epithelial cell layer into the vascular
135 channel and suggested that either dissemination of virions to the endothelial cell layer
136 did not occur, or that infection of the endothelial layer could occur but no viral genomes
137 or infectious virions were released *apically* into the vascular channel by endothelial
138 cells.

139 To address this, we further quantified intracellular viral RNA loads from the total RNA
140 extracted from cells of the apical and vascular channels of three infected LoCs w/o
141 macrophages at 1 dpi. This revealed a significant number of viral transcripts in cells
142 from both the epithelial and endothelial layers (Fig. 2C, Fig. S4C). Additional
143 quantification of intracellular viral RNA from an infected LoC w/o macrophages using
144 a SARS-CoV-2 specific one-step qRT-PCR kit revealed $>10^4$ genomes in both
145 epithelial and endothelial cells (Fig. S4A); genome copy numbers exceeded those for
146 cellular housekeeping gene *RNAseP* (Fig. S4B). Similar numbers of intracellular viral
147 genome copy numbers have been reported for infections of alveolar epithelial cells in
148 monoculture[17] and these numbers are modest in comparison to cells such as airway
149 epithelial cells and Vero E6 cells where SARS-CoV-2 replicates productively [30]. The
150 difference in replication kinetics can also be appreciated from the fact that whereas the
151 *N* gene is most abundant during productive infection in Vero E6 cells [31], we obtained a
152 ratio of SARS-CoV-2 *N* to SARS-CoV-2 *E* <5 (Fig. 2D, Fig. S4D), consistent with the
153 observation of low numbers of extracellular infection virions (Fig. 2B).

154 The detection of SARS-CoV-2 genomes in the endothelial layer within 1 dpi suggests
155 rapid dissemination through *basolateral transfer* from the epithelial to the endothelial
156 layer can occur. Although basolateral transmission has not been reported previously to
157 be the significant mode of transmission for both SARS-CoV-2[32] and SARS-CoV-1[33]

158 infections of monocultures of upper airway cells at the air-liquid interface, this could
159 reflect aspects of infection unique to alveolar epithelial cells, or more generally, of
160 infection of cells where productive infection is rare.
161
162 **SARS-CoV-2 infection of endothelial cells on-chip but not in monoculture alters**
163 **cell morphologies**
164 Recently published autopsy reports of COVID-19 patients revealed features of
165 exudative alveolar damage[12], and a rapid loss of alveolar epithelial cell barrier integrity
166 could account for the basolateral transfer to endothelial cells. The LoC model is
167 compatible with microscopy-based assays, which allowed us to assess changes in
168 cellular physiology with high spatial resolution using confocal microscopy. Even at 3
169 dpi, the epithelial layer maintained a high degree of confluency (Fig, 3D, Fig. S6F),
170 with only a few signs of cell death (Fig. 3D, white arrows). In stark contrast, staining
171 for F-actin localisation revealed striking changes to the morphology of cells in the
172 vascular channel. In comparison to the confluent layer of cells in an uninfected control
173 LoC (3D view in Fig 3A, Fig. S6A) infected LoCs showed profound alterations in
174 endothelial layer architecture (Fig 3B, C). At 2 dpi, cellular clusters characterised by
175 an increased cell density and stronger nucleic acid staining (Fig 3B, yellow arrows)
176 coexisted with areas with normal nucleic acid staining levels but reduced cell-to-cell
177 contact (Fig 3B, white arrows). By 3 dpi, a significant loss of cell confluency was
178 observed (Fig 3C, Fig S6B-D), with large cell clusters no longer visible. To quantify
179 these changes across multiple areas of the chip, we enumerated the number of nuclei
180 per unit area of the membrane surface for infected LoCs at 1 and 3 dpi and uninfected
181 controls. On the epithelial side, the density of nuclei declines progressively due to
182 infection irrespective of the presence (p=0.010, p=9E-4) or absence (p=0.054, p=0.029)

183 of macrophages compared to uninfected controls (Fig. 3E). In contrast, the density of
184 cellular nuclei increases in the endothelial layer at 1 dpi before decreasing back to levels
185 in the control samples at 3 dpi (Fig. 3F), consistent with our observation of the transient
186 formation of endothelial cell clusters. As a further measure of quantification, we
187 measured the proportion of the surface area of the endothelial cell layer with low or no
188 actin staining using a range of intensity thresholds (Fig. S2E). At 3 dpi, a much larger
189 proportion of the surface area of the endothelial layer of infected LoCs had low or no
190 actin staining compared to an uninfected control for all intensity thresholds (Fig. S2E).
191 Immunostaining for the viral S protein at 3 dpi (Fig 3G for endothelial and Fig 3H for
192 epithelial layers, additional examples in Fig. S6B-D, S6F and controls with secondary
193 antibody only in Fig. S8D-G) show clear evidence of individual infected epithelial (Fig.
194 3I) and endothelial cells (Fig. 3J). In some cases, S proteins appear to co-localize with
195 the periphery of the nucleus (Fig. 3I, 3J, white arrows). The transfer of viral proteins
196 from the apical to vascular channel and difference in confluency between the epithelial
197 and endothelial layers at 3 dpi can be better appreciated from a 3D view of the two
198 channels together with the connecting pores in the PDMS membrane; S protein can be
199 clearly localised to the interface of the two cell types in the pores of the membrane
200 (yellow arrows, Fig, 3K). Epithelial and endothelial cells exhibit very different
201 physiological responses to low levels of infection, and vascular damage by 3 dpi was a
202 consistent observation across all infected LoCs (n=12) maintained until 3 dpi in this
203 study
204
205 We next sought to understand if these responses were specific to the lung-on-chip
206 physiology and co-culture, and so examined infections of epithelial and endothelial cell
207 monoculture. At 1 dpi, heavily infected epithelial cells in monoculture with 1000 PFU

208 showed similar levels and intracellular distributions of spike protein (Fig. S5B). In stark
209 contrast, monoculture infections of endothelial cells with viral innocula up to 100-fold
210 greater than the apical inoculum used in the LoC experiments (Fig. 2A) showed few
211 foci of viral S proteins. Endothelial cells retained their morphology and confluency
212 (Fig. S7) up to 2 dpi, in agreement with recent reports of the inability of apical
213 inoculations of SARS-CoV-2 to infect lung microvascular endothelial cells [18]. This
214 suggests that the site of contact of SARS-CoV-2 with endothelial cells (apical vs
215 basolateral) may play an important role – a physiological factor that can be recapitulated
216 in the LoC but not in simpler models.
217
218 **SARS-CoV-2 infected endothelial cells lose expression of tight junction markers**
219 **and adopt a pro-coagulatory phenotype**
220 Actin staining definitively demonstrated the vascular damage caused as a result of loss
221 of cell confluence, we therefore probed cells from both layers in infected and uninfected
222 LoCs for changes in expression of tight junction proteins that might have caused these
223 changes Maximum intensity projections from the epithelial cell layer of an uninfected
224 control showed strong expression of both actin (Fig. 4A) and TJP1 at the cell junctions
225 (Fig. 4B). Similarly, images from a confluent endothelial cell layer in an uninfected
226 control LoC showed actin staining correlated with high expression of Zonula Occludens
227 - 1 (ZO-1 or TJP1) (Fig. 4C) as well as high expression of the endothelial cell specific
228 marker CD31 at cell junctions (Fig. 4D). These results were corroborated by qRT-PCR
229 measurement of high levels of expression of *TJP1* and *CD31* as well as that of VE-
230 cadherin (*CDH5*) in uninfected controls (Fig. S8A).
231 Consistent with Fig. 3, changes to the expression pattern of TJP1 in the epithelial layer
232 at 1 dpi were subtle, TJP1 expression at cell junctions continued to be observed across

233 much of the epithelial cell layer (Fig. 4E, additional images in Fig. S8B, C). SARS-
234 CoV-2 infection, on the other hand, profoundly altered CD31 expression and
235 distribution in the endothelial layer. 3D views of regions of interest in the endothelial
236 layer of an infected LoC showed this to be a dynamic process that resulted in two
237 significant changes: first, an increase in vascular permeability from the loss of tight
238 junctions between CD31+ cells (white arrows in Fig. 4F, G), and second, the presence
239 of cells that showed little or no CD31 expression (Fig. 4F-H). Cells displaying the
240 'CD31- phenotype' typically had higher levels of spike protein (shown in amber in Fig.
241 4F-G), and an increased local cell density and nuclear labelling consistent with the
242 endothelial cell clusters identified in Figure 3. This link is strengthened by examination
243 of zooms of two endothelial cell clusters (Fig. 4I, J, and Fig. 4K, L) from another LoC
244 at 1 dpi. This confirmed that cells in both clusters were CD31- (Fig. 4I, Fig. 4K) but
245 nevertheless express TJP1 and showed strong and altered actin distributions (Fig. 4J,
246 Fig. 4L), morphological features consistent with the clusters identified in independent
247 experiments in Fig. 3. These changes are further corroborated by qRT-PCR
248 measurements which show a progressive and sharp reduction in overall levels of *CD31*
249 and *CDH5* expression in the endothelial layer at 1 dpi and 3 dpi respectively compared
250 to uninfected controls (Fig. 4M). In contrast, the reduction in *TJP1* expression at 1 dpi
251 is less pronounced and expression levels do not decline further at 3 dpi.
252 These dramatic changes in expression of tight junction proteins also resulted in series
253 of complex alterations to the expression of endothelial cell proteins with direct roles in
254 coagulatory pathways (Fig. 4N). For example, infection did not alter expression of *pro-*
255 *coagulatory* Tissue Factor (*F3*) released by endothelial cells as part of the extrinsic
256 coagulation pathway[34], but induced a progressive decrease in the expression of *anti-*
257 *coagulatory* Tissue Factor Pathway Inhibitor (*TFPI*) [35]. A more modest but similarly

258 consistent decrease was also observed for the expression of Thrombomodulin (*THBD*)
259 that also has an anti-coagulatory function. Although infection also decreased the
260 expression of von Willebrand Factor (*VWF*), elevated levels of VWF protein were
261 observed on the surface of the CD31- endothelial cells at 1 dpi via immunofluorescence
262 (bright pink, Fig. 4F-G). In contrast, expression of plasminogen inhibitor activation
263 (PAI-1 expressed by *SERPINE1*) decreased only by 3 dpi. Taken together with the loss
264 of CD31 expression, these results point to the generation of a pro-coagulatory
265 environment in the vascular channel of infected chips.
266

267 **SARS-COV-2 persists in individual epithelial and endothelial cells in the alveolar**
268 **space**

269 Our results thus far showed that infection on-chip itself lead to heterogenous outcomes
270 that were strongly cell-type specific. We therefore performed a series of RNAscope
271 assays with confocal microscopy to probe the spatial distribution and cell-to-cell
272 variability in gene expression at the single-cell level to complement observations from
273 qRT-PCR measurements. We began by examining levels of viral RNA and antisense
274 RNA generated during viral replication *in situ* using probes for *S* RNA and *ORF1AB*
275 antisense RNA respectively. Representative images for 232 x 232 μm^2 fields of view
276 from the apical and vascular channels of chips at 1 and 3 dpi are shown in Fig 5A-H.
277 At 1 dpi, a few examples of heavily infected cells are visible on the epithelial layer (Fig.
278 S9A-C) and viral genomic RNA can be detected throughout the cytoplasm. Consistent
279 with the observations in Fig. S5, such cells are likely to be the source of infectious
280 virions released in the apical wash in Fig. 2A, B. However, in the vast majority of cells
281 on the epithelial layer, the virus is detected only at low levels at 1 dpi (Fig. 5A), and
282 infection does not appear to be limited by (Fig. 5C, white arrows) or even correlated to

283 cellular *ACE2* expression at the time of fixation (Fig. 5D, yellow arrows). Both genomic
284 and antisense RNA are detected in endothelial cells at 1 dpi (Fig. 5B), indicating that
285 intracellular viral replication can also occur in these cells. Heavily infected endothelial
286 cells were not observed, in agreement with the lack of infectious virions in the vascular
287 effluent (Fig. 2C). Endothelial cell clusters are clearly identifiable by their
288 morphological features, and zoomed-in images (Fig 5E, F) show that viral infection of
289 endothelial cells with normal and clustered morphology. As with the epithelial layer,
290 instances of localization of viral RNA with the nucleus is also observed (Fig. 5F, white
291 arrowheads). At 3 dpi, infection in both layers (Fig 5G, 5H) and the loss of endothelial
292 layer integrity is evident (compare Fig. 5G vs. Fig. 5H). We did not detect heavily
293 infected epithelial cells at 3 dpi, in agreement with the diminishing viral titre (Fig. 2A).
294 We normalized the number of RNA dots detected either on a per-cell basis (Fig. 5I-K)
295 or per-field-of-view basis (Fig. S10), to enable quantification of differences between
296 the two layers while accounting for differences in cell numbers and cell death. The
297 median values of intensities were similar across all conditions (Fig. S11). In the
298 epithelial layer, viral infection and replication per cell were either similar (Fig. 5J, L)
299 or lower by 3 dpi (Fig. 5I, p=0.018; Fig. 5K, p=0.006). In contrast, viral RNA
300 accumulates in individual endothelial cells (Fig. 5K, Fig. 5L, p=0.004). The presence
301 of macrophages generally leads to lower levels of viral RNA replication (Fig. 5I, J) but
302 does not prevent the accumulation of viral genomes intracellularly in endothelial cells
303 (Fig. 5L). At 3 dpi, *ACE2* levels are higher on a per-cell basis in endothelial vs epithelial
304 cells (Fig. 5M, p=0.028), due to a reduction in *ACE2* levels on the epithelial layer.
305
306 Normalization on a per-field-of-view basis shows predominantly a *declining* trend for
307 levels of replication (Fig. S10A, B) and intracellular viral RNA (Fig. S10C, D) in both

308 cell types, as well as a *decline* in *ACE2* expression (Fig. S10E), consistent with qRT-
309 PCR measurements (Fig. 1J, Fig. S10F). These results highlight the cumulative effect
310 of differential cell numbers and cell death in these two layers (Fig. 3E, F). Overall, virus
311 levels are low and decline in both layers by 3 dpi, yet the virus persists and continues
312 to replicate within individual infected cells, in agreement with reports of clinical
313 infection.
314
315 **Persistent NF-KB inflammatory responses to SARS-CoV-2 infection in**
316 **endothelial but not epithelial cells**
317 Concurrently, we investigated host responses to the infection. Expression levels of NF-
318 KB related pro-inflammatory genes (*TNFA*, *IL6*, *IL1B*) at 1 dpi was an order of
319 magnitude higher than that of interferon genes in both cell types, with little to no
320 interferon stimulatory gene expression detected in both cell types (Fig. 6A). Responses
321 were also cell-type specific; endothelial cells from infected LoCs showed upregulation
322 of *TNFA*, *IL6* and *IFNB*, *IFNL1* and *IFNL3* genes whereas only expression of *IFNB*
323 and *IFNL1* in epithelial cells were higher than uninfected controls (Fig. 6B). In both
324 cell types, expression of *IP10* and *ISG15* were lower than uninfected controls,
325 consistent with the action of a number of SARS-COV-2 proteins in inhibiting type I
326 interferon signalling [36,37].
327 The LoC platform also allows the simultaneous detection of secreted cytokines in the
328 vascular effluent from the same chips. ELISA assays for IL-1B and IP10 did not detect
329 these cytokines in the effluent (data not shown), the lack of IL-1B secretion despite
330 high expression (Fig. 6B), suggests that it is not exported[38]. IL-6, on the other hand,
331 was consistently detected up to 3 dpi in the vascular effluent from LoCs both in the
332 presence or absence of macrophages (Fig. 6C). No IL-6 was detected in the vascular

333 effluent from uninfected controls. IL-6 levels were not significantly different between
334 these two categories of LoCs, which strongly suggested a non-immune cell source for
335 this cytokine (Fig. 6C).
336 Given the pleiotropic nature of IL-6[39], we also examined expression of the IL6R
337 receptor and the metallopeptidase ADAM17 which sheds the TNF-alpha receptor and
338 the IL-6R receptor[40] in both the epithelial and endothelial layer at 1 dpi (Fig. 6D).
339 Expression of *ADAM17*, which has been shown to enhance vascular permeability[41],
340 was on average 7-fold higher in the endothelial layer at 1 dpi (Fig. 6E), suggestive of
341 the activation of the IL-6 signalling pathway.
342 COVID-19 patients with severe infection have elevated IL-6 levels, and we therefore
343 sought to examine the cell-type specific *IL6* expression at the single cell resolution. We
344 therefore used RNAscope to probe the spatial distribution of *IL6* expression in LoCs
345 reconstituted with macrophages. Consistent with the qRT-PCR data (Fig. S12), *IL6*
346 expression in the control LoC is higher in the epithelial layer (Fig. S13A) than the
347 endothelial layer (Fig. S13B), and immunostaining with an anti-CD45 antibody
348 confirmed that the *IL6* expression in the epithelial layer of the chip did not co-localise
349 with macrophages (Fig. S13A, B). At 1 dpi, individual cells with higher levels of *IL6*
350 expression were observed in both epithelial and endothelial layers (Fig. 6F, G), but only
351 differences in expression in the endothelia layer were statistically significant (Fig. 6J).
352 Cells with high *IL6* expression were also unlikely to be macrophages (Fig. S13 C-E).
353 By 3 dpi *IL6* expression in the epithelial layer had returned to the control levels (Fig.
354 6H, J, S14A) whereas expression increased dramatically and was more widespread in
355 the endothelial layer (Fig. 6I, J, S14A, S14B). Expression did not appear to correlate
356 with level of infection – zooms of cells with comparable levels of infection in Fig. 6I
357 with low (Fig. 6K), medium (Fig. 6L) and high (Fig. 6 M, N) *IL6* expression are shown.

358 Expression in the endothelial layer at 3 dpi was higher than that in the endothelial layer
359 at 1 dpi, the epithelial layer at 3 dpi, and the uninfected controls, both on a per-cell and
360 per-field-of-view basis (Fig. 6J, Fig. S14A, p=0.004, p=0.014, p=0.008 respectively).
361 Unlike viral RNA levels (Fig. S10B, D) *IL6* expression in the endothelial layer *does*
362 *not diminish* over 1-3 dpi and would therefore appear to be the major contributor to IL-
363 6 secretion in the vascular effluent as infection progresses.
364

365 **Inhibition of trans IL-6 signalling reduces but does not eliminate endothelial cell**
366 **inflammation**

367 The activation of IL-6 signalling observed suggested *trans* IL-6 signalling as a potential
368 target to ameliorate the vascular inflammation observed. A similar rationale has led to
369 numerous clinical trials of the anti-IL-6R monoclonal antibody Tocilizumab[42] as a
370 repurposed therapeutic for COVID-19. Tocilizumab administration at 56 μg/mL via
371 continuous perfusion over 2 days post infection *per se* did not abrogate IL-6 secretion,
372 consistent with its mode of action (Fig. 6C). We therefore undertook an investigation
373 of cell morphologies in the endothelial layer of a treated and untreated LoC via actin
374 staining. This revealed that whereas endothelial cell confluency was, on the whole,
375 better retained in the treated chip (Fig. 7A, zooms in Fig. 7B, untreated control in Fig.
376 7D, zoom in Fig. 7E) Tocilizumab administration *did not prevent* the occurrence of
377 endothelial cell clusters (Fig. 7A, zooms in Fig. 7C, untreated control in Fig. 7D, zoom
378 in Fig. 7F). Consistent with these results, immunostaining for CD31 in another treated
379 LoC showed an improvement in the integrity of the endothelial cell layer with tight
380 junctions observable at 2 dpi (3D views in Fig. 7G, H) yet endothelial cell clusters with
381 reduced CD31 expression and strong actin staining were nevertheless formed (3D views
382 in Fig. 7G, H, indicated by yellow arrows).

383

384 To quantify the improvement in permeability, we compared regions of interest (ROIs)
385 that excluded areas of cellular hyperplasia across at least six fields of view from the
386 endothelial layer of LoCs with and without Tocilizumab perfusion, and identified areas
387 with low or no F-actin staining as those with reduced confluence, as in Fig. S6E. A plot
388 of the proportion of pixels with intensities below a defined cut-off threshold (Fig. 7I)
389 showed that the untreated LoC did have a significantly higher proportion of pixels with
390 intensities lower than 5% (p=0.032) of the maximum intensity (p=0.022 for 3% and
391 p=0.038 for 2%). Inhibition of IL-6 signalling through Tocilizumab is therefore able to
392 ameliorate *some* but *not all* of the vascular damage observed.

393

394 **Discussion**

395 The alveolar space has a strikingly different physiology from that of the upper airway.
396 ACE2 is the canonical entry receptor used by SARS-CoV-2, yet is scarce in the alveoli.
397 It has been speculated that high levels of *ACE2* expression may be necessary for export
398 of mature virions [43] and because most virology assays measure viral titre, studies with
399 alveolar epithelial cell lines such as A549 have focused on increasing *ACE2* expression
400 through transfection. In contrast, alternate receptors such as NRP1 more abundant in
401 the lower airways have been understudied, and the effects of uptake via NRP1 vs. ACE2
402 on the viral life cycle is relatively unknown. Here, we populate our model with relevant
403 primary human cells and report low *ACE2* expression and high *NRP1* expression,
404 consistent with human alveolar physiology. Similarly, most infections of alveolar
405 epithelial cells are usually performed at high MOI[16]. Instead, we used an infectious dose
406 that better mimics either a direct inspiration of aerosols or the transfer of infectious
407 virions from the upper respiratory tract. These features, together with the ability to co-

408 culture epithelial cells (at an air-liquid interface) and endothelial cells (under flow)
409 enable the lung-on-chip model to be used to study aspects of early infection that cannot
410 be achieved with other systems.
411
412 Despite low ACE2 expression and low MOI, SARS-CoV-2 infection produced
413 pronounced physiological changes on-chip. This could be due to the high levels of
414 NRP1 and aided by upregulation of *TMPRSS2*, which is known to be important in
415 human SARS-CoV-2 infection. In contrast to models of productive replication, we
416 observe slow intracellular viral replication without significant release of infectious
417 virions, observations that are consistent with reports of recovery of viral RNA in
418 patients after they cease to be infectious[44]. Microscopy-based analyses also revealed
419 that responses to infection are highly heterogenous; for example, the few foci of heavily
420 infected cells might represent cells with constitutively higher levels of *ACE2* expression
421 at the time of infection. However, why alveolar epithelial cells show persistent but not
422 productive infection is still unclear.
423
424 Infection of the epithelial layer rapidly led to an infection of the endothelial layer.
425 Basolateral transmission cannot occur in typical monoculture experiments, but it has
426 not been reported to occur to a large extent in monocultures of airway epithelial cells
427 at the air-liquid interface. However, the basement membrane is much thinner in alveoli
428 than in the upper airway[45], with cell-to-cell contact between the epithelial and
429 endothelial cell layers that is recreated in the array of pores on-chip. Infection of lung
430 microvascular cells therefore might occur through uptake of vesicles as part of cell-to-
431 cell communication between the layers (a receptor-independent mechanism of uptake).
432 These observations are strengthened by the lack of observation of any signs of infection

433 in lung microvascular endothelial cells when directly exposed to the virus on their
434 apical surface. Alternatively, infection of endothelial cells when exposed to the virus
435 basolaterally might still occur due to receptor-mediated uptake, with differences
436 between apical and basolateral infection explained by differences in distribution of cell
437 surface receptors. Notably, NRP1 is likely to be located along the basal surface of the
438 endothelial cells as an integrin-binding protein[26], and SARS-CoV-2 has been shown to
439 infect vascularised organoids, albeit at high MOI[46]. The exact mechanisms remain to
440 be elucidated, but the consequences of this may extend downstream to the persistent
441 infection and endothelial-cell specific cell damage observed.
442
443 A striking feature of SARS-CoV-2 infections in the LoC model was the cell-type
444 specific morphological changes. Infection altered endothelial cell morphology in two
445 different but interconnected ways. First, the loss of tight junctions between cells is
446 indicative of increased vascular permeability that could lead to exudative alveolar
447 damage observed in autopsy reports. Exposed sub-endothelial collagen would likely
448 trigger the contact activation or intrinsic pathway of coagulation. This was also
449 accompanied by pro-coagulatory changes in the extrinsic pathway through a reduction
450 in expression of anti-coagulatory factors such as TFPI and thrombomodulin.
451 Interestingly, infection of Human Umbilical Vein Endothelial Cells (HUVECs) with
452 Dengue virus has been shown to have the opposite effect [47], with a strong increase in
453 thrombomodulin expression consistent with the disease manifestation as a
454 haemorrhagic fever. These results highlight the close link between coagulation and
455 inflammation in this cell type. Second, a subpopulation of endothelial cells completely
456 lost CD31 expression and adopted an altered morphology consisting of cell clusters.
457 These clusters could form either through enhanced proliferation or from cell migration.

458 The former is more likely, as a consistent increase in cell density was observed across
459 multiple LoCs, but both possibilities are consistent with the role of NRP1 as a growth
460 factor receptor or its role in VEGF signalling[48]. The loss of CD31 expression could
461 itself have a number of possible implications: CD31 itself plays important roles in
462 leukocyte migration[49], angiogenesis, in maintaining a anti-coagulatory environment[50,51]
463 as well as preventing endothelial cell death from immune cell mediated inflammation[52].
464 These CD31- cells could further contribute to a pro-coagulatory environment in the
465 microvasculature and lead to changes in vascular architecture reported in autopsies[11].
466 A loss of CD31 expression in endothelial cells will likely alter interactions with
467 neutrophils and platelets that who also express CD31, potentially contributing to the
468 formation of neutrophil extracellular traps and platelet hyperactivity reported in
469 COVID-19[53,54]. These findings are also consistent with the observation of elevated
470 serum levels of CD31 in patients with severe COVID-19[55]. The exact mechanisms for
471 the loss of CD31 and other tight junction markers remains to be elucidated, but a
472 possible mechanism could be through action of viral proteins themselves, as is
473 observed in the case of the K5 protein of the Kaposi Sarcoma herpesvirus[56] that causes
474 Kaposi Sarcoma.
475
476 Increased NF-KB inflammatory responses could also account for the vascular changes
477 observed, and the role of cytokine storms in COVID-19 pathogenesis is still unclear.
478 We observed that low levels of intracellular viral RNA generates an NF-KB mediated
479 pro-inflammatory response, with suppression of antiviral interferon responses,
480 consistent with reports of the effect of a number of viral proteins[57,58]. Within each cell
481 types, there were significant cell-to-cell differences in expression of inflammatory
482 markers, clearly identifiable with single-cell spatial resolution through the use of

483 RNAscope and confocal imaging in the LoC model. These differences could be due to
484 differences in the mode of uptake, or differences in the intracellular localization of viral
485 RNA and RNA replication, or differences in the levels of translation of viral proteins.
486 We observe instances of co-localisation of viral RNA and S protein with the nucleus,
487 which is consistent with bioinformatic predictions using algorithms for RNA
488 localisation[59], but has not been reported in studies using cell lines with productive
489 infections. These atypical sub-cellular localisations may be characteristic of persistent
490 infection and merit further investigation. Yet, once again the responses of epithelial and
491 endothelial cells contrasted sharply – inflammation in epithelial cells was transient,
492 whereas it was persistent in endothelial cells.
493
494 Lastly, given the persistent *IL6* expression in endothelial cells, we applied the model
495 and our microscopy-based approach to examine if Tocilizumab perfusion could the
496 occurrence of either increased vascular permeability or the formation of endothelial cell
497 clusters or both. We found that Tocilizumab *was* able to maintain cellular confluency
498 but did not prevent a subset of endothelial cells from over-proliferating and acquiring
499 an inflammatory phenotype. These observations at the single cell level offer insights
500 into reasons why outcomes with this drug in clinical trials have been modest and at
501 times contradictory[60] and there is insufficient evidence of the efficacy of Tocilizumab
502 in reducing mortality. The lung-on-chip model is therefore able to make clinically
503 testable predictions, highlighting the utility of this approach.
504
505 In sum, SARS-CoV-2 infection of a model of the alveolar space shows a set of unique
506 characteristics underlined by persistent infection, low viral replication, inflammatory
507 response, damage to endothelial barrier integrity, and the formation of a pro-

508 coagulatory environment that are in good agreement with reports of clinical disease.
509 The superior physiological mimicry LoC model (air-liquid interface, co-culture,
510 perfusion through a vascular channel) and high-resolution confocal imaging reveals
511 insights into the dynamics and mechanisms that underlie these observations that are
512 difficult to obtain in other experimental models and that will improve our understanding
513 of the pathogenesis of this multi-organ disease.
514

515 **Acknowledgements**
516 We gratefully acknowledge assistance from Dr Muhammet Fatih Gulen for the ELISA
517 assays. We are also grateful to the members of the BioImaging Core Facility (BIOP)
518 for assistance with confocal microscopy and to Prof Dr Thomas Hugle at the Centre
519 Hospitalier Universitaire Vaudois (CHUV(for donation of Tocilizumab.
520

521 **Methods**

522 Cell culture
523 Primary human alveolar epithelial cells (epithelial cells) and human lung microvascular
524 endothelial cells (endothelial cells) were obtained from a commercial supplier (Cell
525 Biologics, USA). Each vial of epithelial cells comprised a mix of Type I and Type II
526 cells at passage 3, and expression of cell-type specific markers (*AQP5, PDPN,* and
527 *CAV1* for type I and *ABCA3* and *SFTPC* for type II) was verified via qRT-PCR on-
528 chip (Fig. S3D). Both cell types were cultured *in vitro* in complete medium comprising
529 base medium and supplements (Cell Biologics, USA) in 5% CO_2 at 37 °C. Passage of
530 epithelial cells lowered *ACE2* expression (Fig. S2A), therefore all chips were
531 reconstituted with epithelial cells seeded directly on the lung-on-chip (see below),
532 without any additional *in vitro* culture. In contrast, we observed no significant changes
533 in viral entry factor expression in endothelial cells upon passage, and so therefore these
534 cells were passaged between 3-5 times before seeding in the LoC devices.
535

536 PBMC isolation and macrophage differentiation

537 Peripheral blood mononuclear cells were obtained from buffy coat (Interregional Blood
538 Transfusion SRC Ltd, Switzerland) obtained from anonymised donors. PBMCs were
539 isolated using a Biocol Separation procedure as per the manufacturer's instructions.
540 Isolated PBMCs were subsequently cryopreserved in a solution of 70% heat inactivated
541 Fetal Bovine Serum (FBS, Gibco), 20% RPMI Medium (Gibco) and 10%
542 dimethlysulfoxide (DMSO). One week prior to seeding the macrophages in the LoC
543 devices, a cryopreserved aliquot was thawed and cultured in a T-75 flask (TPP,
544 Switzerland) in RPMI supplemented with 10% FBS. CD14+ monocytes were isolated
545 using positive selection (CD14 ultrapure isolation kit, Miltenyi Biosciences) and
546 cultured in RPMI medium supplemented with 10% FBS and differentiated for 7 days
547 with 20 ng/mL recombinant human Macrophage-Colony Stimulating Factor protein
548 (M-CSF) (Thermo Fisher Scientific), and 100U/L of penicillin-streptomycin solution
549 (Thermo Fisher Scientific) to avoid bacterial contamination. The cells were cultured in
550 plastic petri dishes without pre-sterilisation (Greiner Bio-One) so that differentiated
551 macrophages could be more easily detached.
552
553 Quantitative Real-Time PCR (qRT-PCR) for cell characterization
554 Epithelial cells obtained directly from the supplier were grown overnight in cell-culture
555 microdishes (Ibidi) or T-25 cell culture flask (TPP, Switzerland). Passaged epithelial
556 cells were grown to confluency in a T-75 cell culture flask (TPP). Growth media was
557 removed from the flask, and the cells were incubated with the appropriate volume of
558 RNA lysis buffer (RNAeasy Plus Micro Kit, Qiagen) and RNA isolated as per the
559 manufacturer's instructions and resuspended in 25 µL of DEPC-treated water.
560 Approximately 1 µg of RNA was then used to generate cDNA using the
561 SuperScript®IV First-Strand Synthesis System with random hexamers (Invitrogen),
562 which was stored at -20 °C. Specific primers for used for the qRT-PCR are listed in
563 Table S1. qRT-PCR reactions were prepared with SYBR®Green PCR Master Mix
564 (Applied Biosystems) with 500 nM primers, and 1 µL cDNA. Reactions were run as
565 absolute quantification on ABI PRISM®7900HT Sequence Detection System (Applied
566 Biosystems). Amplicon specificity was confirmed by melting-curve analysis.
567
568 Quantitative Real-Time PCR (qRT-PCR) for quantification of viral genomes in the
569 supernatant

570 150 μL of cell-free supernatant was processed using a kit to extract viral RNA as per
571 the manufacturer's instructions (NucleoSpin Dx Virus, Machery Nagel). For the
572 vascular effluent, this was taken from the approximately 1.5 mL of effluent generated
573 daily by the flow through the vascular channel. In the case of the apical wash, the 30
574 μL collected from the apical channel was further diluted in cell culture media up to 150
575 μL and subsequently processed. Viral RNA was eluted in 50mL of DEPC-treated water.
576 5 mL of RNA was then used in a one-step qRT-PCR kit for SARS-CoV-2 detection
577 (2019-nCoV TaqMan RT-PCR kit, Norgen Biosciences) using primer and probe mixes
578 corresponding to the nucleocapsid (N2) gene and the host RNAseP genes. Primer
579 sequences are those listed by the US Centre for Disease Control (CDC).
580
581 Generation of SARS-CoV-2 stocks
582 VeroE6 cells and a clinical isolate of SARS-CoV-2 were a kind gift from the lab of Prof
583 Carolyn Tapparel at the University of Geneva. SARS-CoV2/Switzerland/GE9586/2020
584 was isolated from a clinical specimen in the University Hospital in Geneva in Vero-E6.
585 Cells were infected and supernatant was collected 3 days post infection, clarified,
586 aliquoted and frozen at -80 °C and subsequently titrated by plaque assay in Vero-E6.
587 Virus used for all experiments in this manuscript was at passage 3 in Vero E6 cells.
588
589 Human lung-on-chip (LoC) model
590 LoC made of polydimethylsiloxane (PDMS) were obtained from Emulate (Boston,
591 USA). Extracellular matrix (ECM) coating was performed as per the manufacturer's
592 instructions. Chips were activated using ER-1 solution (Emulate) dissolved in ER-2
593 solution at 0.5 mg/mL (Emulate) and exposed for 20 minutes under UV light. The chip
594 was then rinsed with coating solution and exposed again to UV light for a further 20
595 minutes. Chips were then washed thoroughly with PBS before incubating with an ECM
596 solution of 150 μg/mL bovine collagen type I (AteloCell, Japan) and 30 μg/mL
597 fibronectin from human plasma (Sigma-Aldrich) in PBS buffered with 15 mM HEPES
598 solution (Gibco) for 1-2 hours at 37°C. If not used directly, coated chips were stored
599 at 4°C and pre-activated before use by incubation for 30 minutes with the same ECM
600 solution at 37°C. Endothelial cells were cultured overnight at 37°C and 5% CO_2 in T-
601 75 cell culture flasks, detached with 0.05% Trypsin, concentrated to 5-10 million
602 cells/mL, and seeded on the bottom face of the PDMS membrane. The chip was then

603 incubated for a short period at 37 °C to allow the endothelial cells to spread and
604 subsequently seeded with epithelial cells. Epithelial cells were seeded directly from
605 cryopreserved vials received from the supplier, each vial of 0.5 million cells could be
606 used to seed two chips. To increase reproducibility, vials were pooled and used to seed
607 multiple chips. The chip was incubated overnight with complete epithelial and
608 endothelial media in the epithelial and endothelial channels, respectively, under static
609 conditions. The next day, the chip was washed and a reduced medium for the air-liquid
610 interface (ALI) was flowed through the vascular channel using syringe pumps
611 (Aladdin-220, Word Precision Instruments) at 60 μL/hour as described [61]. The
612 composition of the ALI media used was as described in [61] but with an FBS
613 concentration of 5%. The epithelial face was incubated with epithelial base medium
614 with 1 μM dexamethasone (Sigma Aldrich) without FBS supplementation to promote
615 tight junction formation and surfactant expression as reported in previous lung-on-chip
616 studies[61,62]. Flow was maintained over 2-3 days with daily replacement of the medium
617 on the epithelial face (with dexamethasone supplementation). At the end of this period,
618 in LoCs reconstituted with macrophages, CD14+ macrophages differentiated for 7 days
619 in M-CSF (described above) were detached from the petri dish using 2 mM
620 ethylenediaminetetraacetic acid (EDTA, Sigma Aldrich) in PBS at 4 °C as well as
621 mechanical scraping, centrifuged at 300 *g* for 5 minutes, and resuspended in a small
622 volume of epithelial cell media without dexamethasone. This solution containing
623 macrophages was introduced onto the epithelial face and incubated for 30 minutes at
624 37 °C and 5% CO_2 to allow macrophages to attach to the epithelial cells. Medium on
625 the epithelial face was then removed and the chip was maintained overnight at an air-
626 liquid interface (ALI). Chips were controlled to ensure that they successfully
627 maintained the ALI overnight and were then transferred to the biosafety level 3 (BSL-
628 3) facility for SARS-COV-2 infection. No antibiotics were used in any of the cell
629 culture media for setting up the LoC model.
630
631 <u>Tocilizumab perfusion in the LoC model</u>
632 Tocilizumab/Rho-Actemra (Roche, 20 mg/mL in saline) for intravenous administration
633 were a kind gift from Prof Thomas Hugle at the University Hospital in Lausanne,
634 Switzerland (CHUV). We simulated a single dose of 8 mg/kg given to a person of
635 bodyweight 70 kg and a blood volume of 5 litres to obtain a concentration of 56 μg/mL

636 in the cell culture media. Tocilizumab perfusion was started immediately after infection
637 and was flowed through the vascular channel of infected chips for a period of 2 days
638 post infection.
639
640 Characterization of infection in LoCs
641 Uninfected LoCs were maintained at an ALI for either 1 day (for total RNA extraction
642 (two LoCs without macrophages) or for up to 3 days for RNAscope characterization
643 (one LoC each were reconstituted with and without macrophages) after addition of
644 macrophages, during which time ALI medium was flowed through the endothelial
645 channel at 60 μL/hour. In the case of the former, total RNA from the epithelial and
646 endothelial layers was extracted separately by passing 350 μL of the lysis buffer
647 reconstituted as per the manufacturer's instructions (RNeasy Plus Micro Kit, Qiagen)
648 through easy layer. Complete detachment of the cells in each layer was verified via
649 optical microscopy. RNA was eluted in 25 μL of DEPC-treated nuclease free water and
650 used for subsequent qRT-PCR reactions.
651 In the case of LoCs processed for RNAscope, the chips were fixed for 1 hour using a
652 fresh solution of 4% paraformaldehyde in phosphate buffered saline (PBS), and
653 subsequently dehydrated in a sequence of washes with 50% EtOH, 70% EtOH, and 100
654 % EtOH. The chips were then stored in 100% EtOH at -20 °C until processed for
655 RNAscope at the Histology Cor Facility at EPFL.
656
657 Immunofluorescence characterization
658 For immunofluorescence labelling, the fixed LoCs were incubated with a blocking
659 solution of 2% Bovine Serum Albumin (BSA) in PBS ('blocking buffer'), followed by
660 overnight incubation with the primary antibody in the blocking buffer at 4°C. A list of
661 primary antibodies and concentrations used is included in Table S2. In addition, the
662 infected LoC shown in Fig. 4 E-G was immunostained with Rabbit anti-SARS-CoV
663 spike antisera [63], which was a kind gift of Prof Carolyn Machamer at John Hopkins
664 University. The following day the chip was washed extensively with fresh blocking
665 buffer before inoculation with the secondary antibody at a concentration of 1:300 for 1
666 hour at room temperature. The secondary antibodies used were: Donkey anti-mouse
667 Alexa Fluor 488 (A21206, Thermo Fisher), or Donkey anti-mouse Alexa Fluor 568
668 (A10037, Thermo Fisher), or Donkey anti-mouse Alexa Fluor 647 (A31573, Thermo

669 Fisher), and were chosen to complement the fluorophores already assigned to
670 RNAscope labelling. F-actin on both the epithelial and endothelial face was stained
671 using Sir-Actin dye in the far-red (Spherochrome) at 1 μM for 30 minutes concurrently
672 with Hoechst staining, as described above. Confocal images were obtained on a Leica
673 SP8 microscope in the inverted optical configuration at the EPFL BIOP core facility.
674
675 Infection of the LoC with SARS-CoV-2
676 LoCs for infection were assembled into a sealed Tupperware box modified to contain
677 inlets and outlets for the flow of medium through the vascular channel and was
678 maintained throughout the course of the experiment by use of a syringe pump. On the
679 day of the experiment, an aliquot of virus-containing supernatant was thawed from the
680 stock at -80 °C, and diluted approximately 35-fold in epithelial cell media without FBS
681 to generate the inoculum that corresponded to an infectious dose of 200 – 300 plaque
682 forming units (PFU) in a volume of 30 μL. 30 μL of this solution was then added to the
683 apical channel of each LoC, and the LoC was incubated for an hour at 37°C and 5%
684 CO_2 to enable infection. Thereafter, the medium in the apical channel was removed.
685 The LoC was returned to air-liquid interface and the inlets of the infected chip were
686 sealed with solid pins as a safety precaution. The media flowing through the vascular
687 channel of each LoC was collected in a separate, sealed 15 mL Falcon tube, and each
688 tube was emptied daily, and the effluent stored at -80 °C for further processing. At this
689 time, the metal pins sealing the apical channel of each chip were removed, and 30 μL
690 of epithelial cell media without FBS was briefly added to the channel before being
691 withdrawn and collected as the 'apical wash'. The metal pins were reinserted, and the
692 LoCs returned to the cell culture incubator. Both the vascular effluent and the apical
693 wash from each chip were collected for each day post infection.
694 Infection was terminated at specified time points either by treatment with the lysis
695 buffer for RNA extraction (one LoC reconstituted without macrophages) or by fixing
696 with freshly prepared 4% paraformaldehyde for a period of 1 hour (all other infected
697 LoCs) for RNAscope assay preparation. The chips were then dehydrated as described
698 above and immersed in 100 % EtOH before removal from the BSL-3 facility.
699
700 RNAscope Assay

701 RNAscope Multiplex Fluorescent V2 assay (Bio-techne, Cat. No. 323110) was
702 performed according to manufacturer's protocol directly on chips. They were
703 hybridized with the control Hs 3plex positive control (Bio-techne, Cat. No. 320861) or
704 a combination of the following probes V-nCoV2019-orf1ab-sense (Bio-techne, Cat.
705 859151), Hs-ACE2-C2 (Bio-techne, Cat. 848151-C2), V-nCoV2019-S-C3 (Bio-
706 techne, Cat. 848561-C3), HS-Il1b-C1 (Bio-techne, Cat. 310361), and Hs-Il6-C2 (Bio-
707 techne, Cat. No. 310371-C2) simultaneously at 40°C for 2 hours. The different channels
708 were revealed with TSA Opal570 (Akoya Biosciences, Cat. No. FP1488001KT), TSA
709 Opal650 (Akoya Biosciences, Cat. No. FP1488001KT) and TSA Opal690 (Akoya
710 Biosciences, Cat. No. FP1497001KT). Cells were counterstained with DAPI and
711 mounted with Prolong Gold Antifade Mountant (Thermo Fisher, P36930).
712
713 ELISA assays
714 Frozen vascular effluent from infected chips was thawed, incubated at 58 °C for 30
715 minutes to ensure sterilization, and then removed from the BSL-3 for further
716 processing. Levels of human IL-6 were determined by enzyme-linked immunosorbent
717 assays (BD Biosciences) as per the manufacturers' instructions.
718
719 Confocal imaging and Image Analysis
720 Infected and control LoCs were imaged using a Leica SP8 confocal microscope with a
721 white light laser. For chips processed via RNAscope and labelled with Opal 650 and
722 Opal 690, the excitation and emission windows were carefully chosen to minimise
723 overlap of signal. LoCs were imaged with a 25x water immersion objective (NA=0.95,
724 Leica), with standard settings across chips labelled the same way. Z stacks were
725 subsequently deconvolved using the Huygens Deconvolution Software (Scientific
726 Volume Imaging) and 3D views were rendered using the FIJI ClearVolume plugin[64].
727 Custom-written software in MATLAB was used to segment and identify the 3D
728 volume, mean intensity, and number of RNA dots in each field of view using the
729 nestedSortStruct algorithm for MATLAB written by the Hughey Lab
730 (https://www.github.com/hugheylab/nestedSortStruct, GitHub). Statistical analysis
731 was performed using Origin 9.2 (OriginLabs) and P-values were calculated using a
732 Kruskal-Wallis one-way ANOVA test, with the null hypothesis that the medians of
733 each population were equal.
734 **Data availability statement**

735 The datasets generated during and/or analysed during the current study are available
736 from the corresponding authors on reasonable request. Software code used to analyse
737 these datasets will be uploaded to Zenodo prior to publication
738
739 **References**

740 1. Bhatia, S. N. & Ingber, D. E. Microfluidic organs-on-chips. *Nat. Biotechnol.*
741 **32**, 760–772 (2014).
742 2. Thacker, V. V *et al.* A lung-on-chip infection model reveals protective and
743 permissive roles of alveolar epithelial cells in tuberculosis. *bioRxiv*
744 2020.02.03.931170 (2020) doi:10.1101/2020.02.03.931170.
745 3. Villenave, R. *et al.* Human Gut-On-A-Chip Supports Polarized Infection of
746 Coxsackie B1 Virus In Vitro. *PLoS One* **12**, e0169412 (2017).
747 4. Ortega-Prieto, A. M. *et al.* 3D microfluidic liver cultures as a physiological
748 preclinical tool for hepatitis B virus infection. *Nat. Commun.* **9**, 1–15 (2018).
749 5. Grassart, A. *et al.* Bioengineered Human Organ-on-Chip Reveals Intestinal
750 Microenvironment and Mechanical Forces Impacting Shigella Infection. *Cell*
751 *Host Microbe* **26**, 435-444.e4 (2019).
752 6. Torrelles, J. B. & Schlesinger, L. S. Integrating Lung Physiology, Immunology,
753 and Tuberculosis. *Trends Microbiol.* **25**, 688–697 (2017).
754 7. Gattinoni, L. *et al.* COVID-19 does not lead to a "typical" acute respiratory
755 distress syndrome. *American Journal of Respiratory and Critical Care*
756 *Medicine* vol. 201 1299–1300 (2020).
757 8. Marini, J. J. & Gattinoni, L. Management of COVID-19 Respiratory Distress.
758 *JAMA - Journal of the American Medical Association* vol. 323 2329–2330
759 (2020).
760 9. Yao, Y. *et al.* D-dimer as a biomarker for disease severity and mortality in

761 COVID-19 patients: A case control study. *J. Intensive Care* **8**, 49 (2020).
762 10. Messner, C. B. *et al.* Ultra-High-Throughput Clinical Proteomics Reveals
763 Classifiers of COVID-19 Infection. *Cell Syst.* **11**, 11-24.e4 (2020).
764 11. Ackermann, M. *et al.* Pulmonary vascular endothelialitis, thrombosis, and
765 angiogenesis in Covid-19. *N. Engl. J. Med.* **383**, 120–128 (2020).
766 12. Carsana, L. *et al.* Pulmonary post-mortem findings in a series of COVID-19
767 cases from northern Italy: a two-centre descriptive study. *Lancet Infect. Dis.*
768 (2020) doi:10.1016/S1473-3099(20)30434-5.
769 13. Teuwen, L. A., Geldhof, V., Pasut, A. & Carmeliet, P. COVID-19: the
770 vasculature unleashed. *Nature Reviews Immunology* vol. 20 389–391 (2020).
771 14. Lang, M. *et al.* Pulmonary Vascular Manifestations of COVID-19 Pneumonia.
772 *Radiol. Cardiothorac. Imaging* **2**, e200277 (2020).
773 15. Claudio, D. *et al.* Acute Lung injury evolution in Covid-19. *medRxiv*
774 2020.08.09.20170910 (2020) doi:10.1101/2020.08.09.20170910.
775 16. Blanco-Melo, D. *et al.* Imbalanced Host Response to SARS-CoV-2 Drives
776 Development of COVID-19. *Cell* **181**, 1036-1045.e9 (2020).
777 17. Hui, K. P. Y. *et al.* Tropism, replication competence, and innate immune
778 responses of the coronavirus SARS-CoV-2 in human respiratory tract and
779 conjunctiva: an analysis in ex-vivo and in-vitro cultures. *Lancet Respir. Med.* **8**,
780 687–695 (2020).
781 18. Hou, Y. J. *et al.* SARS-CoV-2 Reverse Genetics Reveals a Variable Infection
782 Gradient in the Respiratory Tract. *Cell* **182**, 429-446.e14 (2020).
783 19. Nawroth, J. C. *et al.* A Microengineered Airway Lung Chip Models Key
784 Features of Viral-induced Exacerbation of Asthma. *Am. J. Respir. Cell Mol.*
785 *Biol.* **63**, 591–600 (2020).

786 20. Huang, J. *et al.* SARS-CoV-2 Infection of Pluripotent Stem Cell-derived
787 Human Lung Alveolar Type 2 Cells Elicits a Rapid Epithelial-Intrinsic
788 Inflammatory Response. *bioRxiv* 2020.06.30.175695 (2020)
789 doi:10.1101/2020.06.30.175695.
790 21. Abo, K. M. *et al.* Human iPSC-derived alveolar and airway epithelial cells can
791 be cultured at air-liquid interface and express SARS-CoV-2 host factors.
792 *bioRxiv* 2020.06.03.132639 (2020) doi:10.1101/2020.06.03.132639.
793 22. Youk, J. *et al.* Robust three-dimensional expansion of human adult alveolar
794 stem cells and SARS-CoV-2 infection. *bioRxiv* **2**, 2020.07.10.194498 (2020).
795 23. Qi, F., Qian, S., Zhang, S. & Zhang, Z. Single cell RNA sequencing of 13
796 human tissues identify cell types and receptors of human coronaviruses.
797 *Biochem. Biophys. Res. Commun.* **526**, 135–140 (2020).
798 24. Hikmet, F. *et al.* The protein expression profile of ACE2 in human tissues.
799 *Mol. Syst. Biol.* **16**, (2020).
800 25. Song, J. *et al.* Upregulation of angiotensin converting enzyme 2 by shear stress
801 reduced inflammation and proliferation in vascular endothelial cells. *Biochem.*
802 *Biophys. Res. Commun.* **525**, 812–818 (2020).
803 26. Valdembri, D. *et al.* Neuropilin-1/GIPC1 Signaling Regulates α5β1 Integrin
804 Traffic and Function in Endothelial Cells. *PLoS Biol.* **7**, e1000025 (2009).
805 27. Daly, J. L. *et al.* Neuropilin-1 is a host factor for SARS-CoV-2 infection.
806 *bioRxiv* 2020.06.05.134114 (2020) doi:10.1101/2020.06.05.134114.
807 28. Cantuti-Castelvetri, L. *et al.* Neuropilin-1 facilitates SARS-CoV-2 cell entry
808 and provides a possible pathway into the central nervous system. *bioRxiv*
809 2020.06.07.137802 (2020) doi:10.1101/2020.06.07.137802.
810 29. Hoffmann, M. *et al.* SARS-CoV-2 Cell Entry Depends on ACE2 and

811 TMPRSS2 and Is Blocked by a Clinically Proven Protease Inhibitor. *Cell* **181**,
812 271-280.e8 (2020).
813 30. Chu, H. *et al.* Comparative tropism, replication kinetics, and cell damage
814 profiling of SARS-CoV-2 and SARS-CoV with implications for clinical
815 manifestations, transmissibility, and laboratory studies of COVID-19: an
816 observational study. *The Lancet Microbe* **1**, e14–e23 (2020).
817 31. Kim, D. *et al.* The Architecture of SARS-CoV-2 Transcriptome. *Cell* **181**, 914-
818 921.e10 (2020).
819 32. V'kovski, P. *et al.* Disparate temperature-dependent virus – host dynamics for
820 SARS-CoV-2 and SARS-CoV in the human respiratory epithelium. *bioRxiv*
821 2020.04.27.062315 (2020) doi:10.1101/2020.04.27.062315.
822 33. Tseng, C.-T. K. *et al.* Apical Entry and Release of Severe Acute Respiratory
823 Syndrome-Associated Coronavirus in Polarized Calu-3 Lung Epithelial Cells.
824 *J. Virol.* **79**, 9470–9479 (2005).
825 34. Zelaya, H., Rothmeier, A. S. & Ruf, W. Tissue factor at the crossroad of
826 coagulation and cell signaling. *J. Thromb. Haemost.* **16**, 1941–1952 (2018).
827 35. Mast, A. E. Tissue Factor Pathway Inhibitor: Multiple Anticoagulant Activities
828 for a Single Protein. *Arteriosclerosis, Thrombosis, and Vascular Biology* vol.
829 36 9–14 (2016).
830 36. Xia, H. *et al.* Evasion of Type I Interferon by SARS-CoV-2. *Cell Rep.* **33**,
831 108234 (2020).
832 37. Miorin, L. *et al.* SARS-CoV-2 Orf6 hijacks Nup98 to block STAT nuclear
833 import and antagonize interferon signaling. *Proc. Natl. Acad. Sci. U. S. A.* **117**,
834 28344–28354 (2020).
835 38. Lopez-Castejon, G. & Brough, D. Understanding the mechanism of IL-1β

836 secretion. *Cytokine and Growth Factor Reviews* vol. 22 189–195 (2011).
837 39. Tanaka, T., Narazaki, M. & Kishimoto, T. Il-6 in inflammation, Immunity, And
838 disease. *Cold Spring Harb. Perspect. Biol.* **6**, 16295–16296 (2014).
839 40. Zunke, F. & Rose-John, S. The shedding protease ADAM17: Physiology and
840 pathophysiology. *Biochimica et Biophysica Acta - Molecular Cell Research*
841 vol. 1864 2059–2070 (2017).
842 41. Dreymueller, D. *et al.* Lung endothelial ADAM17 regulates the acute
843 inflammatory response to lipopolysaccharide. *EMBO Mol. Med.* **4**, 412–423
844 (2012).
845 42. Tanaka, T., Narazaki, M., Ogata, A. & Kishimoto, T. A new era for the
846 treatment of inflammatory autoimmune diseases by interleukin-6 blockade
847 strategy. *Seminars in Immunology* vol. 26 88–96 (2014).
848 43. Klein, S. *et al.* SARS-CoV-2 structure and replication characterized by in situ
849 cryo-electron tomography. *bioRxiv* 2020.06.23.167064 (2020)
850 doi:10.1101/2020.06.23.167064.
851 44. Cevik, M. *et al.* SARS-CoV-2, SARS-CoV, and MERS-CoV viral load
852 dynamics, duration of viral shedding, and infectiousness: a systematic review
853 and meta-analysis. *The Lancet Microbe* (2020) doi:10.1016/S2666-
854 5247(20)30172-5.
855 45. Weibel, E. R. On the Tricks Alveolar Epithelial Cells Play to Make a Good
856 Lung. *Am. J. Respir. Crit. Care Med.* **191**, 504–513 (2015).
857 46. Monteil, V. *et al.* Inhibition of SARS-CoV-2 Infections in Engineered Human
858 Tissues Using Clinical-Grade Soluble Human ACE2 In Brief Clinical-grade
859 recombinant human ACE2 can reduce SARS-CoV-2 infection in cells and in
860 multiple human organoid models. Inhibition of SARS-CoV-2 Infections in

861 Engineered Human Tissues Using Clinical-Grade Soluble Human ACE2. *Cell*
862 **181**, 905-913.e7 (2020).
863 47. Jiang, Z., Tang, X., Xiao, R., Jiang, L. & Chen, X. Dengue virus regulates the
864 expression of hemostasis-related molecules in human vein endothelial cells. *J.*
865 *Infect.* **55**, e23–e28 (2007).
866 48. Guo, H. F. & Vander Kooi, C. W. Neuropilin functions as an essential cell
867 surface receptor. *Journal of Biological Chemistry* vol. 290 29120–29126
868 (2015).
869 49. Newman, P. J. & Newman, D. K. Signal transduction pathways mediated by
870 PECAM-1: New roles for an old molecule in platelet and vascular cell biology.
871 *Arteriosclerosis, Thrombosis, and Vascular Biology* vol. 23 953–964 (2003).
872 50. Zhang, J. J., Kelm, R. J., Biswas, P., Kashgarian, M. & Madri, J. A. PECAM-1
873 modulates thrombin-induced tissue factor expression on endothelial cells. *J.*
874 *Cell. Physiol.* **210**, 527–537 (2007).
875 51. Falati, S. *et al.* Platelet PECAM-1 inhibits thrombus formation in vivo. *Blood*
876 **107**, 535–541 (2006).
877 52. Cheung, K. *et al.* CD31 signals confer immune privilege to the vascular
878 endothelium. *Proc. Natl. Acad. Sci. U. S. A.* **112**, E5815–E5824 (2015).
879 53. Zuo, Y. *et al.* Neutrophil extracellular traps in COVID-19. *JCI Insight* **5**,
880 (2020).
881 54. Manne, B. K. *et al.* Platelet gene expression and function in patients with
882 COVID-19. *Blood* **136**, 1317–1329 (2020).
883 55. Li, L. *et al.* Serum levels of soluble PECAM-1 in COVID-19 patients are
884 associated with disease severity. *J. Infect. Dis.* (2020)
885 doi:10.1093/infdis/jiaa642.

886 56. Mansouri, M. *et al.* Kaposi sarcoma herpesvirus K5 removes CD31/PECAM
887 from endothelial cells. *Blood* **108**, 1932–1940 (2006).
888 57. Hadjadj, J. *et al.* Impaired type I interferon activity and inflammatory responses
889 in severe COVID-19 patients. *Science (80-.).* eabc6027 (2020)
890 doi:10.1126/science.abc6027.
891 58. Thoms, M. *et al.* Structural basis for translational shutdown and immune
892 evasion by the Nsp1 protein of SARS-CoV-2. *Science* (2020)
893 doi:10.1126/science.abc8665.
894 59. Wu, K., Zou, J. & Chang, H. Y. RNA-GPS Predicts SARS-CoV-2 RNA
895 Localization to Host Mitochondria and Nucleolus. *bioRxiv Prepr. Serv. Biol.*
896 2020.04.28.065201 (2020) doi:10.1101/2020.04.28.065201.
897 60. Parr, J. B. Time to Reassess Tocilizumab's Role in COVID-19 Pneumonia.
898 *JAMA Internal Medicine* (2020) doi:10.1001/jamainternmed.2020.6557.
899 61. Hassell, B. A. *et al.* Human Organ Chip Models Recapitulate Orthotopic Lung
900 Cancer Growth, Therapeutic Responses, and Tumor Dormancy In Vitro. *Cell*
901 *Rep.* **21**, 508–516 (2017).
902 62. Huh, D. *et al.* Reconstituting organ-level lung functions on a chip. *Science* **328**,
903 1662–8 (2010).
904 63. McBride, C. E., Li, J. & Machamer, C. E. The Cytoplasmic Tail of the Severe
905 Acute Respiratory Syndrome Coronavirus Spike Protein Contains a Novel
906 Endoplasmic Reticulum Retrieval Signal That Binds COPI and Promotes
907 Interaction with Membrane Protein. *J. Virol.* **81**, 2418–2428 (2007).
908 64. Royer, L. A. *et al.* ClearVolume: Open-source live 3D visualization for light-
909 sheet microscopy. *Nature Methods* vol. 12 480–481 (2015).
910

915 **Figures**

916

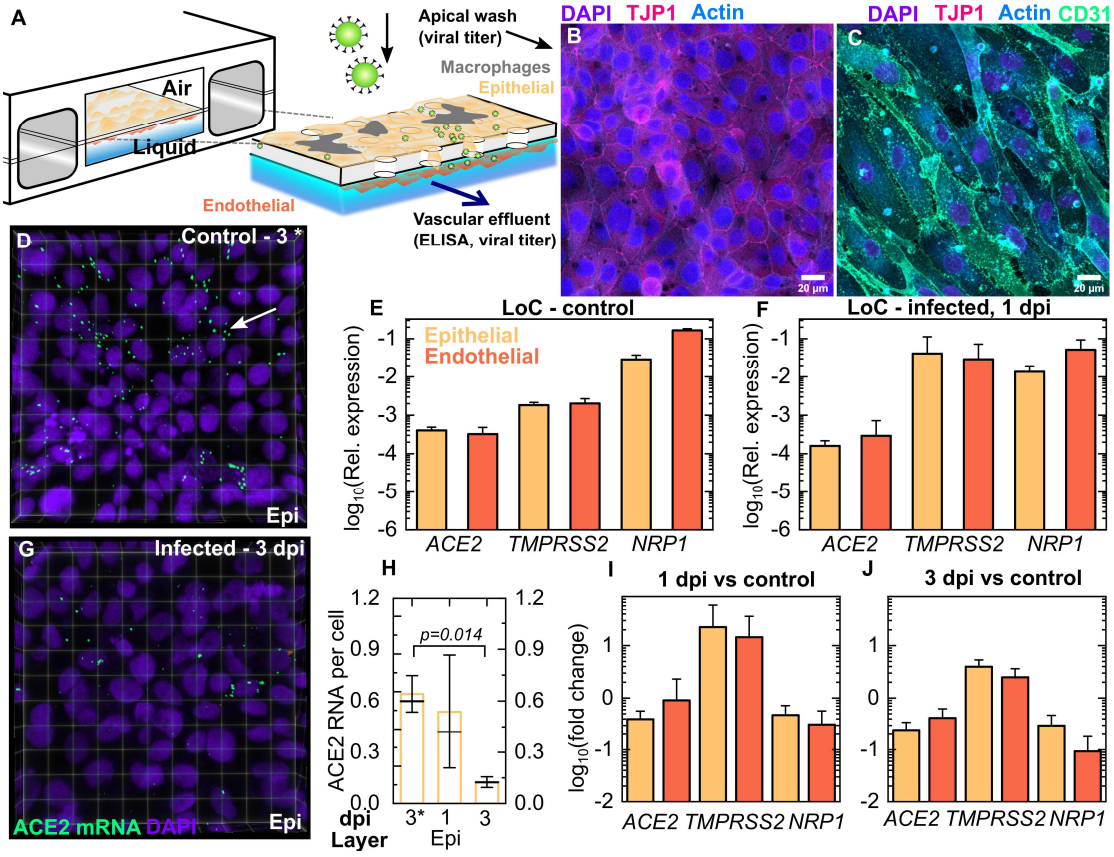

917

918 **Fig. 1. SARS-CoV-2 infection in a human lung-on-chip model.**

919 (**A**) Schematic of the LoC model for SARS-CoV-2. Maximum intensity projections
920 show that confluent layers of epithelial and endothelial cells with strong expression of
921 tight junction markers populate the top (**B**) and bottom faces (**C**) of the porous
922 membrane. Actin, CD31, TJP-1 and nuclear labelling are shown in azure, spring green,
923 bright pink, and electric indigo LUTs respectively. qRT-PCR characterization of the
924 epithelial and endothelial layers on-chip for SARS-CoV-2 entry markers (*ACE2,*
925 *TMPRSS2, NRP1*) for cells extracted from the apical and vascular channels from n=3
926 uninfected LoCs (**E**) and n=4 infected LoCs at 1 day-post infection (**F**). In both cases
927 expression is normalized to *GAPDH* levels. *ACE2* levels were also characterized using
928 RNAscope, a representative 3D view of a 232 x 232 μm^2 field of view of the epithelial
929 face of an uninfected control at 3 days at air-liquid interface (3C) (**D**) and infected LoC

930 at 3 dpi (**G**) are shown. The nuclear labelling is indicated in electric indigo and *ACE2*
931 mRNA is labelled in spring green LUT. (**H**) *ACE2* expression decreases between 1and
932 3 dpi in the LoC model, quantified on a per-cell basis for 4-5 fields of view across one
933 control and one infected chip at each timepoint. (**I, J**) A plot of the fold change in
934 expression of host proteins required for viral entry at 1 day-post infection (n=4 LoCs)
935 and 3 days-post infection (n=2 LoCs) vs. uninfected controls (n=3 LoCs). The bars
936 represent the mean value, the solid line represents the median value, and the error bars
937 represent the standard deviation. P-values are calculated using a Kruskal-Wallis one-
938 way ANOVA test.
939

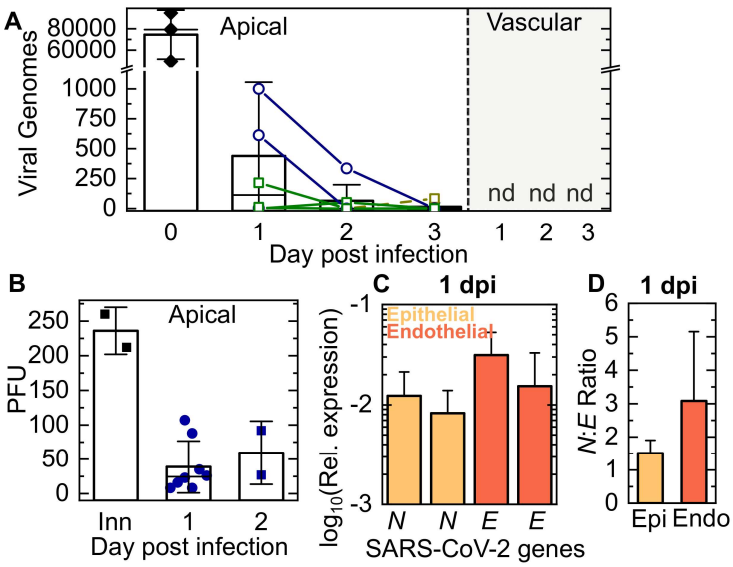

Fig. 2. Viral replication but lack of release of infectious virions characterizes SARS-CoV-2 infection in the LoC model.

The kinetics of release of SARS-CoV-2 progeny was assessed from samples obtained from a wash of the apical face of the chip (**A, B**), and the vascular effluent (**A**) collected at each day-post infection. (**A**) The number of viral genomes in each sample was quantified using a one-step qRT-PCR assay for the SARS-CoV-2 N gene. The starting inoculum introduced to the apical side (labelled 'Inn') corresponded to 200-300 PFU. Lines join datapoints from the same LoC, reconstituted with (green squares) and without (dark blue circles) macrophages. Viral genome numbers within the apical wash showed a declining trend over 3 days of infection. Viral genomes are not detected ('nd') in the vascular effluent for all the chips shown. (**B**) Measurements of plaque forming units (PFU) from the apical wash of LoCs reconstituted without macrophages (n=8 for 1 dpi, n=2 for 2 dpi) confirms the presence of infectious virions. (**C**) Quantification of the intracellular levels of transcripts for the SARS-CoV-2 *N* and SARS-CoV-2 *E* genes in the epithelial and endothelial layers of infected LoCs at 1 dpi (n=3) relative to expression of the eukaryotic housekeeping gene *GAPDH*. (**D**) SARS-CoV-2 *N* : SARS-CoV-2 *E* ratio in the epithelial and endothelial layers of the infected LoCs shown in

958 (**C**). In all plots, the bars represent the mean value and the error bars represent the
959 standard deviation, the solid black line in (**A**) represents the median.
960
961

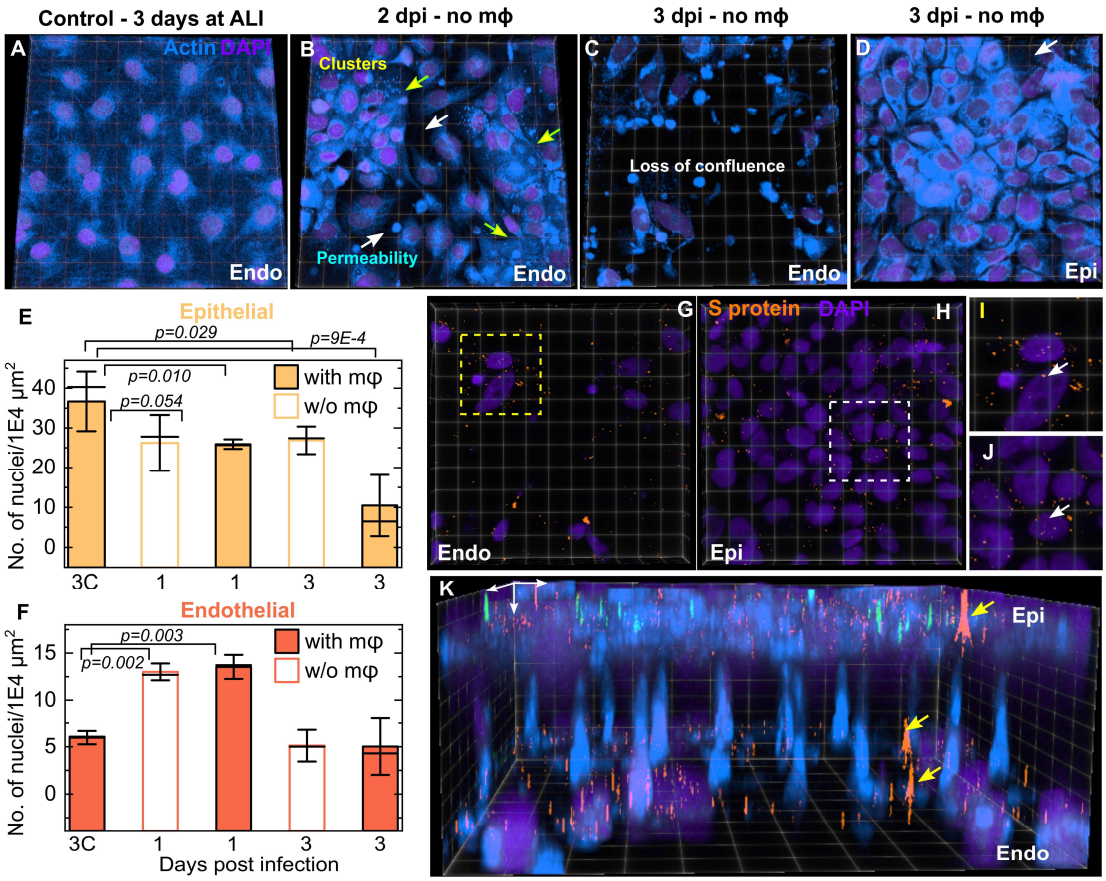

Fig. 3. SARS-CoV-2 infection rapidly disrupts confluency of the endothelial layer. (**A-D**) 3D views of representative 232 x 232 μm^2 (**A, B**) and 155 x 155 μm^2 (**C, D**) fields of view from confocal imaging of an uninfected control (**A**), and infected chips without macrophages at days 2 (**B**) and 3 (**C, D**) post infection respectively. Actin and nuclear labelling are shown in azure and indigo, respectively. (**B**) At 2 dpi, adjacent areas of endothelial cell clusters identified by a stronger nuclear stain and brighter actin staining (yellow arrows) and cells with increased permeability and loss of confluence (white arrows) are indicated. (**C**) At 3 dpi, a significant loss of barrier integrity is observed in the endothelial layer, whereas the epithelial layer directly above this field of view (**D**) is relatively intact. A small area of missing cells in the epithelial layer is indicated with a white arrow in (**D**). Plots of density of nuclei (number of nuclei per 1E4 μm^2) on the epithelial (**E**) and endothelial (**F**) faces of infected LoCs both with and without macrophages for characterization of the cellular layer integrity. The bars

976 represent the mean value, the solid line represents the median and the error bars
977 represent the standard deviation from at least 4 fields of view each from two
978 independent LoCs for each timepoint. Data from uninfected controls corresponding to
979 the 3 dpi timepoint are labelled '3C'. The fields of view in (**C, D**) are shown also in
980 (**G, H**) respectively, SARS-CoV-2 spike (S) proteins labelled via immunofluorescence
981 are false-colored in amber. Zooms in (**I**) and (**J**) show clear evidence of intracellular
982 spike protein within both endothelial and epithelial cells, respectively. (**K**) A 3D view
983 of the field of views in (**C, D**) and (**G, H**) respectively highlights the relative damage
984 to the endothelial layer versus the epithelium, as well as the basolateral transmission of
985 S protein via junctions in the pores of the membrane (identified with white arrows). P-
986 values are calculated using a one-way Kruskal-Wallis ANOVA test.

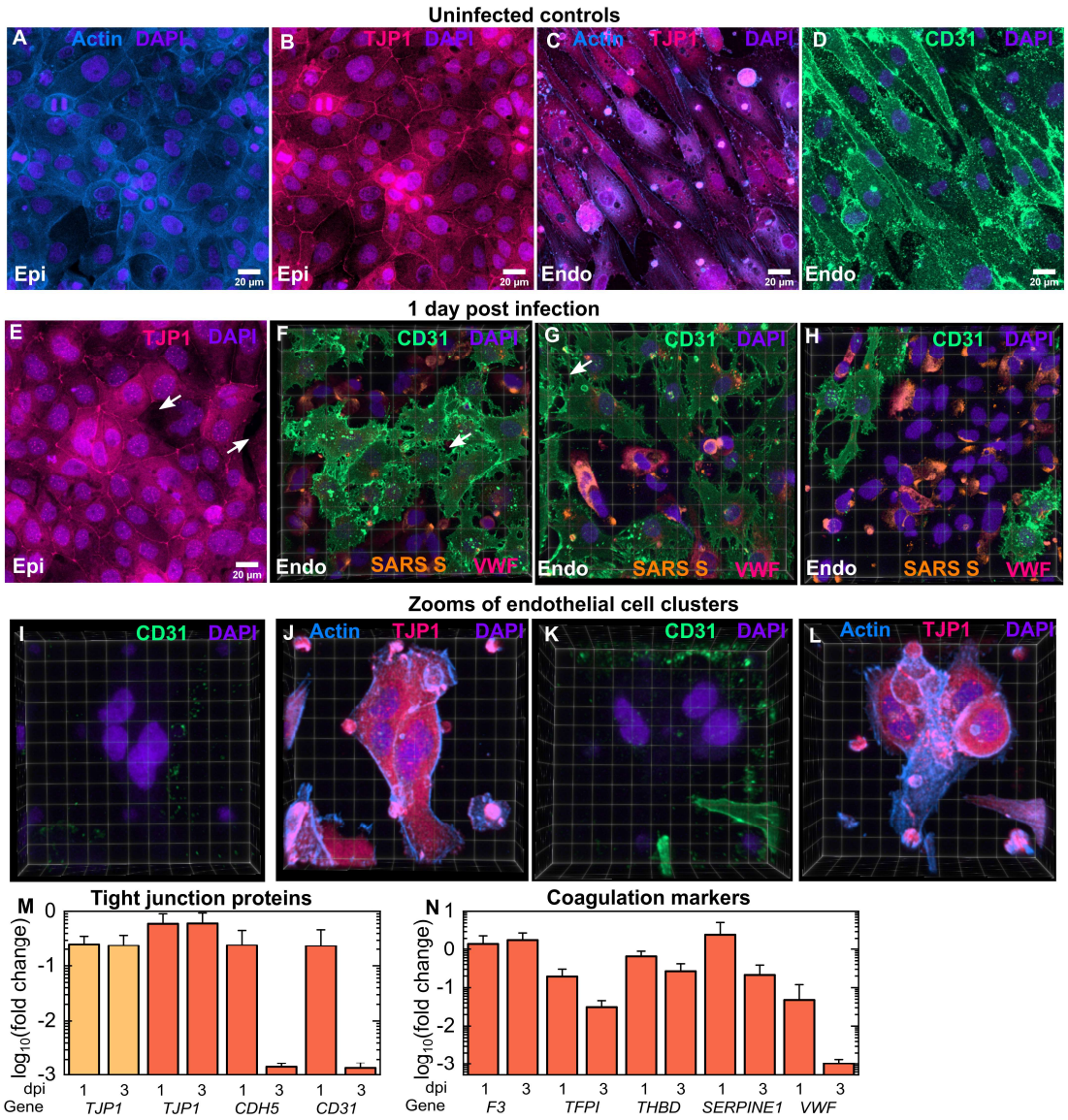

Fig. 4. SARS-CoV-2 infection leads to a loss of tight junctions, generation of CD31-endothelial cell clusters and a pro-coagulatory environment.

(**A-D**) Maximum intensity projects of 232 x 232 μm^2 fields of view from the epithelial (**A**, **B**) and endothelial layers of an uninfected control LoC. Epithelial cells show strong actin (**A**) and TJP1 expression (**B**, identified via antibody staining) at the cell junction boundaries. Endothelial cells also show high levels of TJP-1 expression (**C**) together with CD31 expression at cell junctions (**D**, identified via antibody labelling). Actin, TJP-1, CD31, and nuclear labelling are indicated with the azure, bright pink, spring green and electric indigo LUTs respectively. 3D views of one 232 x 232 μm^2 field of

997 view of the epithelial (**E**) and (**F-H**) three 232 x 232 μm^2 fields of view of the
998 endothelial layers of an infected LoC at 1 dpi. Areas with lower TJP1 expression in the
999 epithelial layer in (**E**) are indicated by white arrows. (**F-H**) Areas with loss of tight
1000 junctions between cells on the endothelial surface is indicated by white arrows. The
1001 proportion of the surface area covered by confluent cells decreases sequentially from
1002 (**F**) to (**H**). Endothelial cell clusters with no CD31 expression are clearly visible and the
1003 proportion of the surface area covered by these clusters increases sequentially from (**F**)
1004 to (**H**). In (**F-H**), spike protein is identified via an anti-SARS-spike antibody and shown
1005 in amber LUT, and von Willebrand Factor identified by antibody labelling is shown in
1006 bring pink LUT. Zooms of two endothelial cell clusters (**I, J** and **K, L**) in the endothelial
1007 layer of another infected LoC at 1 dpi confirm that little or no CD31 expression is
1008 detected (**I**, **K**) despite high levels of actin and TJP-1 protein expression in these cells.
1009 (**J**, **L**). (**M**) Plot of the fold change in expression of *TJP1* (epithelial and endothelial
1010 layers) and *TJP1*, *CDH5*, and *CD31* (endothelial layers only) in infected LoCs at 1 dpi
1011 (n=3) vs, uninfected controls (n=3). (**N**) Plot of the fold change in gene expression of
1012 endothelial cell specific coagulation markers - Tissue Factor (*F3*), Tissue Factor
1013 Pathway Inhibitor (*TFPI*), Thrombomodulin (*THBD*), Plasminogen Activator Inhibitor
1014 (*SERPINE1*) and von Willebrand Factor (*VWF*) in infected LoCs at 1 dpi (n=3) vs.
1015 uninfected controls (n=3). In all plots, bars represent the mean value and error bars
1016 represent the standard deviation.
1017

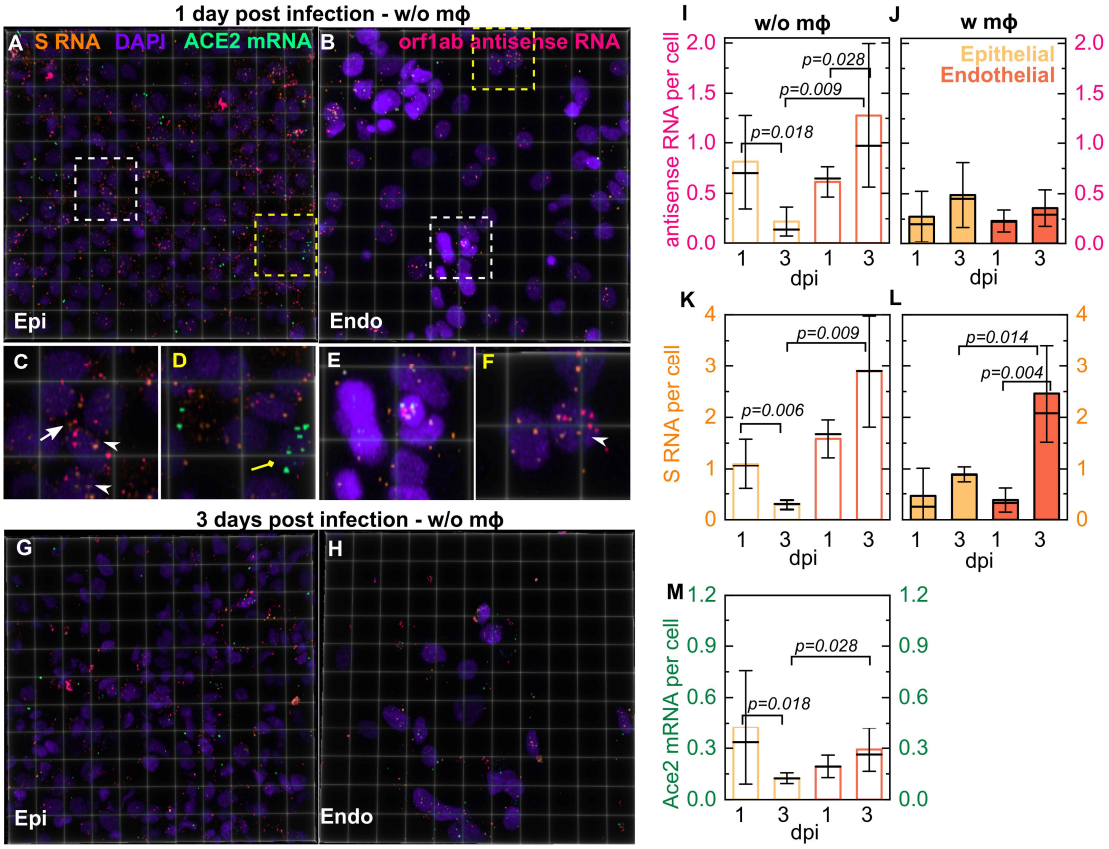

Fig. 5. RNAscope analysis reveals intracellular localization and slow accumulation of intracellular viral RNA in the LoC model.

3D views of 232 x 232 μm^2 fields of view of the epithelial (**A, G**) and endothelial layer (**B, H**) from infected LoCs reconstituted without macrophages at 1 (**A, B**) and 3 dpi (**G, H**). *Orf1ab* antisense RNA, *S* RNA, *ACE2* mRNA, and nuclear staining with DAPI are false-colored pink, amber, spring green, and electric indigo, respectively. (**C, D**) Zooms corresponding to the region in (**A**) highlighted with white and yellow boxes, respectively. (**C**) An example of infection and intracellular replication in a cell with no detectable *ACE2* expression (white arrow) as well as nuclear localization of viral RNA (white arrowhead). (**D**) An example of an uninfected cell with *ACE2* mRNA expression (yellow arrow). (**E, F**) Zooms corresponding to the regions in (**B**) representing increased nucleic acid staining (hyperplasic) and normal levels of nucleic acid staining highlighted with white and yellow boxes, respectively. (**E**) Examples of infection of hyperplasic endothelial cells both with and without *ACE2* expression (**F**) Examples of

1033 endothelial cell infection with no *ACE2* expression, nuclear localization of viral RNA
1034 in an infected endothelial cell is indicated (white arrowheads). Quantification of viral
1035 antisense RNA (**I, J**) and viral genomic RNA (**K, L**) from pairs of otherwise identical
1036 LoCs reconstituted without (**I, K**) and with macrophages (**J, L**) analyzed at 1 and 3 dpi.
1037 Plots show the number of spots normalized by the total number of cells in 4-6 field of
1038 views detected using RNAscope and confocal imaging using identical imaging
1039 conditions for all chips. Bars represent the mean value, the solid line represents the
1040 median, and error bars represent the standard deviation. (**M**) Quantification of *ACE2*
1041 expression per cell in epithelial cells and endothelial cells in LoCs reconstituted without
1042 macrophages at 1 and 3 dpi respectively. P-values are calculated using a Kruskal-Wallis
1043 One-Way ANOVA Test.
1044

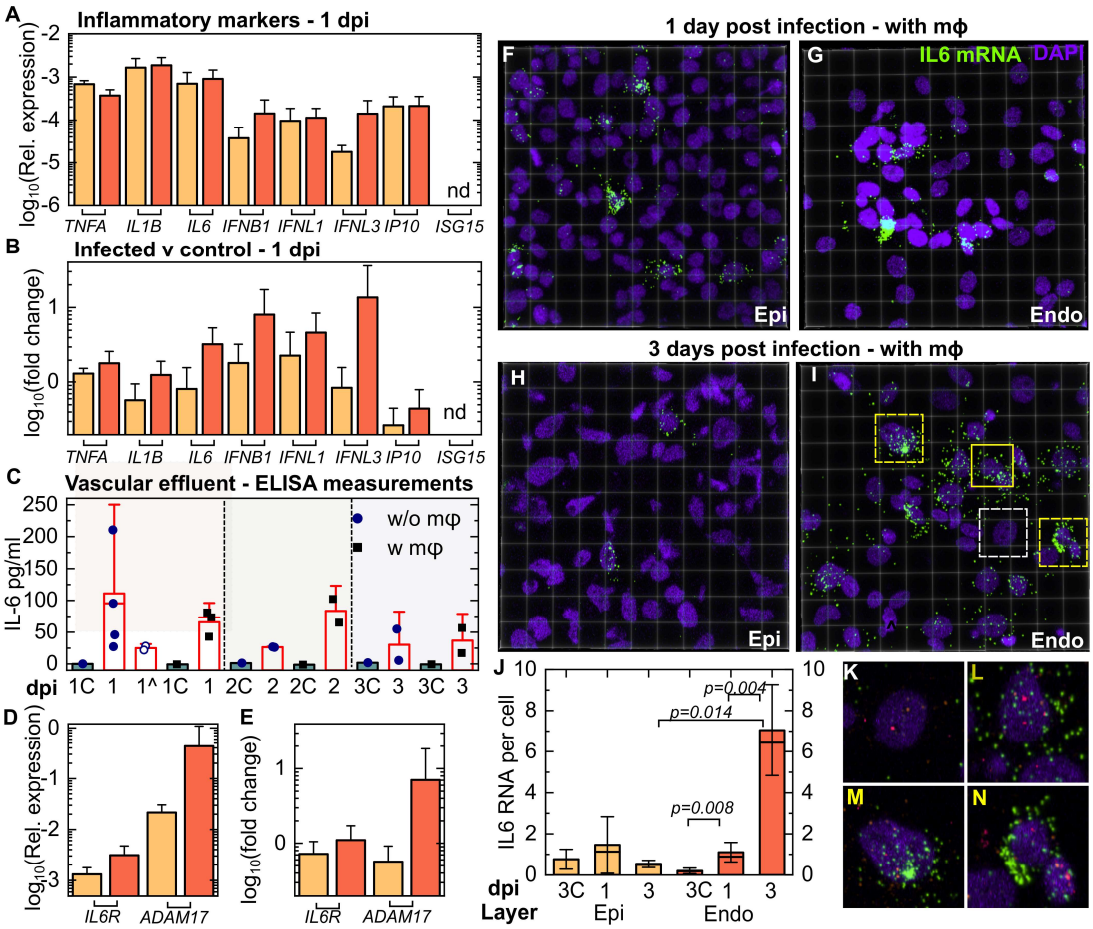

Fig. 6. SARS-CoV-2 infection generates a persistent pro-inflammatory response in endothelial cells.

(**A**) Expression relative to *GAPDH* of pro-inflammatory cytokines (*TNFA, IL1B, IL6)*, interferon genes (*IFNB, IFNL1, IFNL3*) and interferon stimulating genes (*IP10, ISG15*) in the epithelial and endothelial layer of infected LoCs at 1 dpi reconstituted without macrophages (n=3 for *IFNL1* and *IFNL3* in the epithelial layer, n=4 for all other data). (**B**) Fold-change in the markers in (**A**) relative to uninfected controls (n=3) (data in Fig. S12) at the same timepoint. The bar represents the mean and the error bars the standard deviation. (**C**) Enzyme-linked immunosorbent assay (ELISA) measurements for IL-6 in the vascular effluent for at least two infected LoCs at each timepoint reconstituted with and without macrophages. Uninfected controls for each condition are labelled with a 'C' and grey bars, and LoCs with Tocilizumab administration are indicated by ^. The height of the bars represents the mean, the median is represented by a solid line, and

1059 the error bars represent the standard deviation. Each dot represents the mean of two
1060 technical replicates. (**D**) Expression of *IL6R* and *ADAM17* relative to *GAPDH* in the
1061 epithelial and endothelial layer of infected LoCs at 1 dpi (n=3 for the epithelial layer
1062 and n=4 for endothelial layer). (***E***) Fold-change in expression relative to uninfected
1063 controls (n=3 for both layers). (**F-I**) 3D views of representative 232 x 232 μm^2 fields of
1064 view of the epithelial (**F, H**) and endothelial layer (**G, I**) from infected LoCs
1065 reconstituted with macrophages at 1 (**F, G**) and 3 dpi (**H, I**). *IL6* mRNA, and nuclear
1066 staining are indicated with the chartreuse and electric indigo LUTs respectively. (**K-N**)
1067 Zooms corresponding to the regions in (**I**) highlighted with white (**K**) and yellow boxes
1068 with solid (**L**) and dashed lines (**M**, **N**) respectively. In these panels, *orf1abantisense*
1069 RNA (pink) and *S* RNA (amber) are also shown. The panels show examples of cells
1070 with similar levels of viral infection but with no (**K**), intermediate (**L**) and high levels
1071 (**M, N**) of *IL6* expression. (**J**) Quantification of *IL6* expression in epithelial and
1072 endothelial cells from a pair of otherwise identical LoCs analyzed at 1 and 3 dpi,
1073 respectively. Plots show the total number of spots normalized by the number of cells in
1074 4-6 fields of view detected using RNAscope assay using identical imaging conditions
1075 for all chips. Bars represent the mean value, the solid line represents the median, and
1076 error bars represent the standard deviation. Data from uninfected controls for 3 days at
1077 air-liquid interface is indicated by 'C'. The bar represents the mean and the error bars
1078 the standard deviation. P-values are calculated using a Kruskal-Wallis One-Way
1079 ANOVA Test.
1080
1081

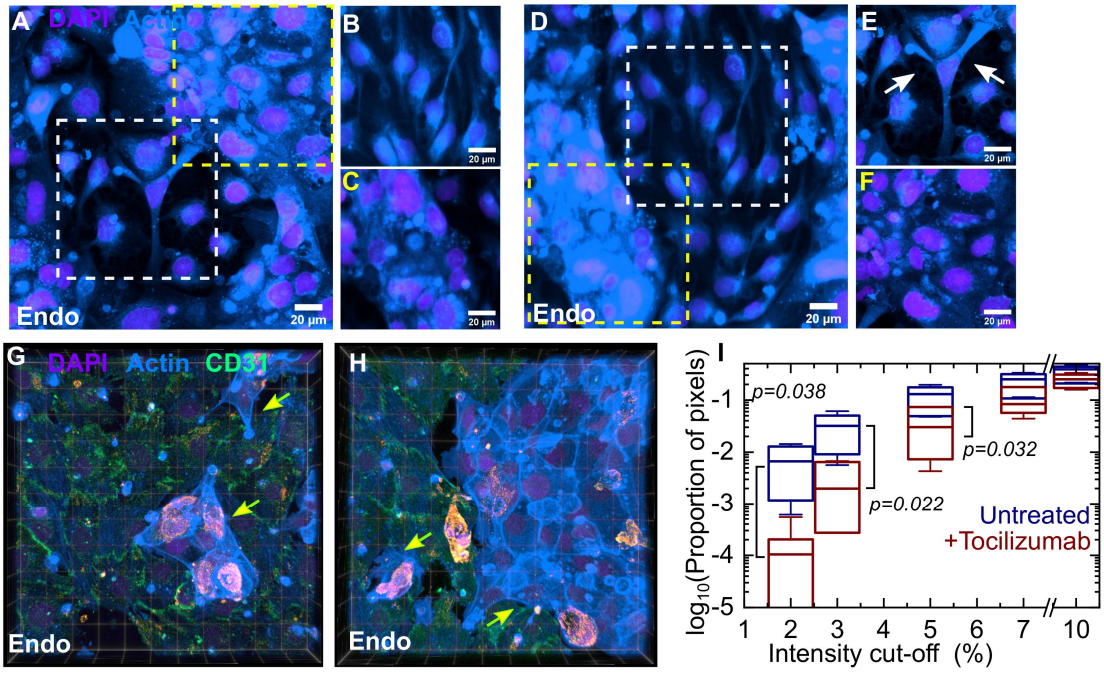

Fig. 7. Tocilizumab treatment reduces vascular permeability but does not prevent formation of endothelial cell clusters with reduced *CD31* expression.

Maximum intensity projections of representative 232 x 232 µm^2 fields of view of the endothelial layer from an infected LoC reconstituted without macrophages at 2 dpi with (**A**) and without Tocilizumab treatment (**D**). Actin and nuclear staining are indicated with the azure and electric indigo LUTs respectively, the actin staining is saturated for the endothelial cell clusters to highlight cells with lower levels of actin. (**B, C**) Zooms corresponding to the region in (**A**) highlighted with white and yellow boxes, respectively. (**B**) A region with normal vascular profile, (**C**) A region of endothelial cell cluster formation with increased actin staining. (**E, F**) Zooms corresponding to the regions in (**D**) representing regions highlighted with white and yellow boxes, respectively. (**E**) An example of reduced tight junctions between endothelial cells; bare patches are indicated with arrows. (**F**) A region of endothelial cell clusters. (**G**) 3D views from two 232 x 232 mm2 field of views of the endothelial layer of a Tocilizumab treated infected LoC at 2 dpi, immunostaining for the tight junction protein CD31 is shown in the Spring Green LUT. Endothelial cell clusters with low CD31 expression

1099 and altered actin staining are also visible and indicated by yellow arrows. (**I**) A plot of
1100 the proportion of pixels (shown on a logarithmic scale) with regions of low F-actin
1101 intensity identified via cut-off thresholds defined as a percentage of the maximum
1102 intensity in 6-7 regions of interest each for LoCs with and without Tocilizumab
1103 administration. ROIs were chosen from 232 x 232 μm^2 fields of view and were defined
1104 to exclude the occurrence of hyperplasic cells. A significantly larger fraction of the
1105 surface area of the ROIs for the untreated chips have low F-actin intensities. P-values
1106 are calculated using a Kruskal-Wallis One-Way ANOVA Test.
1107
1108